Theoretical Predictions vs Environmental Observations on Serpentinization Fluids: Lessons from the Samail Ophiolite in Oman

J. A. M. Leong[1,2], A. E. Howells[1,3], K. J. Robinson[1,4], A. Cox[5], R. V. Debes II[1,2], K. Fecteau[1,4], P. Prapaipong[1,2], and E. L. Shock[1,2,4]

[1]Group Exploring Organic Processes In Geochemistry (GEOPIG), Arizona State University, Tempe, AZ 85287, USA

[2]School of Earth & Space Exploration, Arizona State University, Tempe, AZ 85287, USA

[3]School of Life Sciences, Arizona State University, Tempe, AZ 85287, USA

[4]School of Molecular Sciences, Arizona State University, Tempe, AZ 85287, USA

[5]Laboratory Exploring Geobiochemical Engineering and Natural Dynamics (LEGEND), Montana Technological University, Butte, MT 59701, USA

Corresponding author: J. A. M. Leong (jmleong@asu.edu)

Key Points:

1. Serpentinizing fluids from the Oman ophiolite were sampled and analyzed to test thermodynamic predictions with environmental observations
2. Compositions of a few fluid samples can be accounted for by equilibrium thermodynamic predictions
3. Most samples deviate from equilibrium expectations and can be accounted for by simulations of additional processes (*e.g.*, fluid mixing)

Abstract

Thermodynamic calculations provide valuable insights into the reactions that drive the profound fluid transformations during serpentinization, where surface fluids are transformed into some of the most reduced and alkaline fluids on Earth. However, environmental observations usually deviate from thermodynamic predictions, especially those occurring at low temperatures where equilibrium is slowly reached. In this work, we sampled and analyzed >100 low-temperature (<40°C) fluids from the Samail ophiolite in Oman to test thermodynamic predictions with environmental observations. Additional simulations (*e.g.*, fluid mixing, mineral leaching) were also conducted to account for deviations from equilibrium expectations. Type 1 circumneutral (pH 7 to 9) fluids result from fluid interactions with completely serpentinized rocks common in the shallow subsurface. Type 2 hyperalkaline (pH >11) fluids approach equilibrium with diopside, and serpentine and brucite actively forming during advanced stages of serpentinization. We also investigated fluids with pH values of 9 to 11 to test whether these fluids are indicative of intermediate stages of serpentinization or mixing between the above end-member fluids. Fluids at intermediate stages of serpentinization and fluids derived from mixing can have the same pH, but the former have considerably lower dissolved Si that can be attributed to concomitant subsurface serpentinization and mineral carbonation processes. Overall, this work demonstrates that predicted and measured compositions of serpentinization-derived fluids can be successfully reconciled using a combination of equilibrium and fluid-transport simulations. This work substantiates these calculations as useful tools in exploring serpentinization reactions in deep subsurface aquifers on Earth as well as those beyond our own planet.

Plain Language Summary

The lithosphere is directly involved in the habitability of a planet. Interaction between water and rocks mobilizes nutrients and facilitates the transfer of energy from the lithosphere to the biosphere. Of all water and rock reactions on Earth, perhaps one of the most profound is *serpentinization* as it produces some of the most reduced and alkaline fluids on the planet. Fluids generated through serpentinization support microbial communities and thus are attractive for their potential to support life in the deep subsurface as well as in rocky bodies outside our own planet. Thermodynamic simulations allow predictions of the compositions of fluids and microbial energy supplies in these less accessible serpentinizing environments. However, deviations from predictions will likely occur, especially at low temperatures where equilibrium is slowly reached. We sampled and analyzed >100 fluids from the Samail ophiolite in Oman to test equilibrium expectations with environmental observations. Further simulations that can reconcile predicted fluid compositions with actual measurements were also conducted. By demonstrating that simulations of low-temperature serpentinization can be successfully applied to analogous processes here on Earth, this work substantiates these calculations as useful tools in exploring serpentinization reactions occurring beyond our own planet.

1. Introduction

When surface water meets ultramafic rocks, reactions occur that ultimately generate some of the most alkaline and reduced fluids on Earth. This process, known as *serpentinization*, involves the hydrous mineral serpentine mainly replacing the anhydrous minerals olivine and pyroxene that originally composed ultramafic rocks. During serpentinization, fluids become H_2-rich through the coupled oxidation of ferrous iron to ferric iron in minerals and reduction of water to hydrogen. Ultimately, the enormous redox disequilibria generated when these reduced fluids mix with oxic surface fluids provide energy to drive many metabolic reactions (McCollom, 2007; Amend et al., 2011; Schrenk et al., 2013; Canovas et al., 2017) and the synthesis of organic compounds (Shock and Canovas, 2010; Lang et al., 2010). Geochemical energy supplies for microbial life make serpentinizing systems attractive model ecosystems for assessing the link between the geosphere and the biosphere, including those occurring in the Earth's subsurface (Schrenk et al., 2013; Klein et al., 2015; Rempfert et al., 2017; Fones et al., 2019) and possibly, in other rocky bodies in our solar system (Schulte et al., 2006; Vance et al., 2007; Holms et al., 2015; Glein and Zolotov, 2020). The alkaline and reduced environments resulting from serpentinization are also proposed to have facilitated the emergence of life on Earth (*e.g.*, Russell et al., 1994, 2010; Sleep et al., 2004; Holm et al., 2006; Martin and Russell, 2007; Martin et al., 2008; Russell, 2018).

Submarine vents releasing >100°C fluids to the ocean, such as those in the Lost City (~120°C, Kelley et al., 2001; Seyfried et al., 2015) and Rainbow vent fields (~360°C, Charlou et al., 2002), are famous examples of serpentinizing environments, known for their towering chimneys and vigorous vents surrounded by diverse deep-sea biological communities. Less conspicuous, but likely far more widespread, are fluids seeping diffusively from ultramafic rocks

91 at temperatures <100°C, such as those found near spreading ridges (Früh-Green et al., 2018),
92 serpentine mud volcanoes near subduction zones (Mottl et al., 2003, 2004; Wheat et al., 2008;
93 2020; Mottl, 2009), and ultramafic bodies in continents, where serpentinization-generated fluids
94 are documented in ophiolites, ultramafic massifs, metamorphic belts, and kimberlite fields in ~20
95 countries (for a list of these studies, see Etiope and Whiticar, 2019 and Leong and Shock, 2020).
96 The common occurrence of serpentinized fluids in many continental settings where ultramafic
97 rocks and water can interact illustrates that serpentinization can actively proceed even at ambient
98 conditions (25°C, 1 bar).

99 Mass-transfer calculations based on thermodynamic equilibrium provide insights into
100 reactions that can drive the transformation of surface fluids such as rain and seawater into
101 reduced, high-pH fluids. When applied, past studies (Pfeifer, 1977; Bruni et al., 2002; Palandri
102 and Reed, 2004; Cipolli et al., 2004; Sader et al., 2007; Boschetti and Toscani, 2008; Marques et
103 al., 2008; Okland et al., 2012; Paukert et al., 2012) show that mass-transfer calculations can
104 account for the overall compositional trends of ultramafic-hosted fluids even at low-temperature
105 conditions. However, at low temperatures where equilibrium is slowly reached, deviations from
106 predictions can occur. Fluid compositions that deviate from equilibrium expectations have not
107 been a focus of previous theoretical studies but can inform us of the various fluid transport
108 processes that may contribute to assessing the habitability of the serpentinizing subsurface.
109 Serpentinization is not unique to Earth and can occur in other rocky bodies in the solar system
110 such as Mars (Schulte et al., 2006; Ehlmann et al., 2010) and ice-covered ocean worlds in the
111 outer solar system like Europa and Enceladus (Vance et al., 2007; Glein et al., 2015; Waite et al.,
112 2017; Glein and Zolotov, 2020). With limited existing data, and in preparation for future
113 sampling, expectations for the compositional variabilities of fluids and microbial communities

possible in these less accessible environments can be informed by thermodynamic simulations. It is thus imperative that we test thermodynamic simulations in accessible and analogous low-temperature serpentinizing systems here on Earth to assess their utility in predicting consequences of serpentinization in other planetary bodies. In this study, we test predictions on fluid compositions by recent calculations of Leong and Shock (2020) with fluids sampled from the Samail ophiolite in the Sultanate of Oman.

The Samail ophiolite hosts some of the largest and best preserved continental exposures of ultramafic rocks (Nicolas et al., 2001) as well as several low-temperature (<40°C), hyperalkaline fluids that were documented by numerous studies in the past (Barnes et al., 1978; Neal and Stanger, 1983; 1984; 1985; Bath et al., 1987; Taylor et al., 1991; Sano et al., 1993; Dewandel et al., 2005; Matter et al., 2006; Paukert et al., 2012; 2019; Chavagnac et al., 2013a; 2013b; Boulart et al., 2013; Ollson et al., 2014; Miller et al., 2016; Rempfert et al., 2017; Canovas et al., 2017; Vacquand et al., 2018; Zgonnik et al., 2019; Fones et al., 2019; Giampouras et al., 2020; Boyd et al., 2020). To test thermodynamic predictions, we sampled and analyzed 138 compositionally diverse fluids from 17 locations in the ophiolite with pH values ranging from near-neutral to hyperalkaline.

We investigated reactions that account for fluids with end-member compositions: (1) near-neutral and (2) hyperalkaline pH. The former have pH values ranging from 7 to 9, are enriched in Mg^{+2} and HCO_3^-, and typically occur in shallow aquifers and surface streams. In contrast, the latter are highly alkaline (pH >11) and enriched in Ca^{+2}, OH^-, and gases such as H_2 and/or CH_4. Hyperalkaline fluids occur mainly in deeper aquifers (>500 m) and manifest at the surface when deep-seated fluids discharge as springs (Dewandel et al., 2005). We also examined fluids with intermediate pH (9 to 11), which have been less of a focus in previous studies, to

assess if they are consequences of the serpentinization pathway where meteoric water is transformed into hyperalkaline fluids, or if they result from mixing between the end-member fluids. A field-based method to identify these fluid types is also proposed that can help inform decisions involving exploration, sampling, and experiments while in the field. Ultimately, through the aid of predictions, we can quantify the contributions of various stages of serpentinization to observed fluid compositions. Eventually, these calculations, tested with analogous processes at Earth's surface, can provide constraints for the exploration of low-temperature serpentinizing environments such as those construed for the deep and early Earth, as well as in other rocky bodies in our Solar System.

2. Methods

2.1. Computational Model

Thermodynamic reaction-path calculations simulate reactions of minerals with a fluid and determine the compositions of coexisting solid phases and fluid constituents attained at equilibrium at various extents of the overall reaction progress. Details on the model setup are described in Leong and Shock (2020) and are summarized in the supporting materials accompanying this work. In addition to reaction-path calculations, dissolved concentrations of solutes as constrained by mineral solubilities were also predicted, as described in detail in the supplementary materials.

2.2. Field and Analytical Methods

2.2.1. Field Sites

A total of 138 fluid samples were taken from nine surface (springs) and eight subsurface (wells) sites in the Samail ophiolite in 2009, 2010, 2012, and 2014. Locations of these sampling sites in the Samail ophiolite are shown in Figure 1. All sites are hosted in ultramafic rocks except

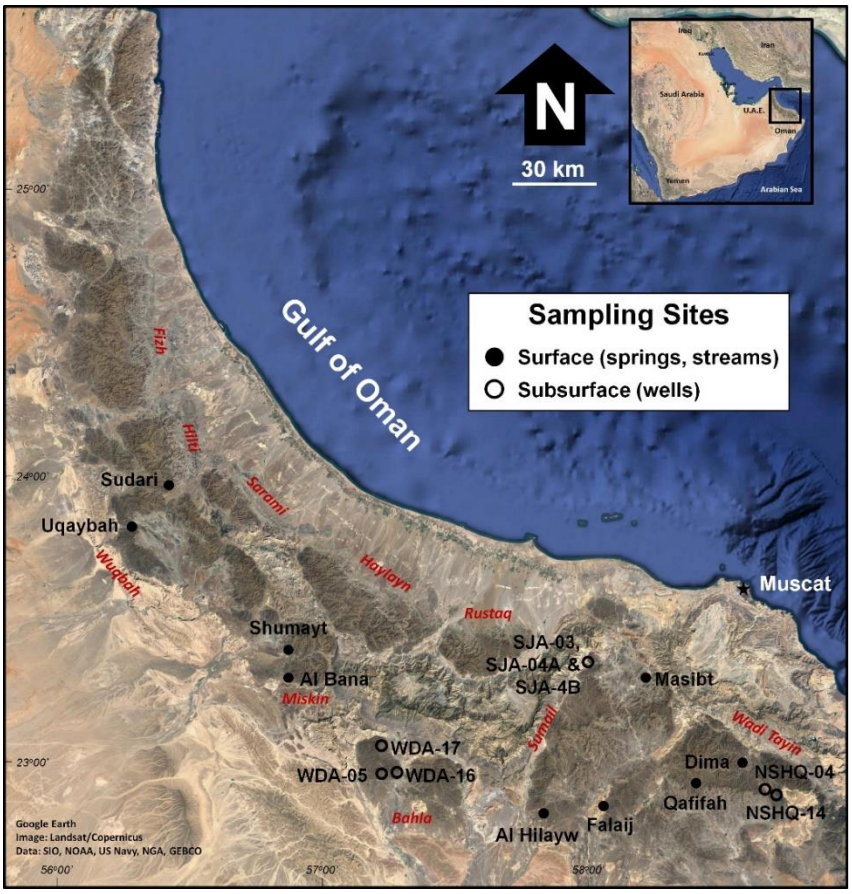

Figure 1. Locations of sample sites overlain on a satellite map of the Oman ophiolite (Google Earth). Filled black circles represent sites where fluids were sampled from the surface (springs, streams) while open circles represent sites where fluids were sampled from wells. Names of the various massifs that comprise the ophiolite are indicated in red texts.

for WDA-16 and Masibt, which are located within a gabbroic body. The occurrence of hyperalkaline fluids at most sites can be associated with geologic structures (basal thrust and lithological boundaries) that can promote flow of deep-seated fluids to the surface through fractures. Three sites (Al Hilayw, Falaij, and Al Bana) are in outcrops close to the base of the ophiolite (basal thrust) corresponding to where the ophiolite is thrust over the Arabian Peninsula. The other sites are located within the ophiolite and many are hosted in ultramafic rocks near the ultramafic-gabbro transition. The 17 sites are distributed across several of the massifs that comprise the Samail ophiolite. Sites at Dima, Qafifah, and Falaij, together with the wells NSHQ-

174 04 and NSHQ-14, are in the Wadi Tayin Massif. Masibt and wells SJA-03, SJA-04A, and SJA-
175 04B are in the northern part of the Samail Massif, while Al Hilayw is further south in the same
176 massif. All of the above locations are in the southern portion of the Samail ophiolite, while wells
177 WDA-05, WDA-16, and WDA-17 (Bahla Massif), sites Shumayt and Al Bana (Miskin Massif),
178 Uqaybah (Wuqbah Massif), and Sudari (Hilti Massif) are in the central part of the Samail
179 ophiolite. Hyperalkaline springs in Masibt, Dima, Qafifah, Uqaybah, Sudari, and Shumayt are
180 seeping at or close to stream beds (Figures 2a and 2b), sometimes comprising a major component
181 of the stream flow as shown in Figure 2c. In contrast, those located near the basal thrust seep
182 from the flanks of ultramafic outcrops with no apparent associated surface stream flows in the
183 vicinity. Where possible, at each surface site and well, three fluid types were sampled: (1)
184 circumneutral to slightly alkaline fluids (pH 7–9), (2) hyperalkaline fluids (pH >11), and (3)
185 fluids with intermediate pH (pH 9–11).

186

187 Figure 2. Hyperalkaline pools covered in white calcite films flowing into surface streams at (a)
188 Qafifah and (b) Dima. (c) Hyperalkaline fluids comprising a major component of the stream flow
189 at Shumayt.

190 2.2.2. Field and Analytical Methods

191 Portable electrodes and meters were used for *in situ* measurements of pH, temperature,
192 and conductivity. pH electrodes (WTW™ SenTix™ 41 gel electrode) attached to meters
193 (WTW™ 3300*i* and 3110) were calibrated daily using 7.0, 10.01 and 12.46 pH buffers.
194 Temperature and conductivity were measured using a YSI 30 handheld meter. Samples were
195 filtered in the field (Pall Acrodisc® 32 mm PF syringe filter with 1.2 and 0.8/0.2 μm Supor®
196 membrane) and stored in containers for further laboratory analyses. Measurements of redox-
197 sensitive species (dissolved ferrous iron, O_2, sulfide, nitrate, and ammonia) were performed on-
198 site using field spectrophotometers (Hach® 2400) with commercially supplied reagents from
199 Hach®. All analyses, except dissolved O_2 and sulfide, were measured using filtered water
200 samples. Dissolved ferrous iron concentrations were measured using the 1,10 phenanthroline
201 method. Total dissolved nitrate and ammonia concentrations were determined using the cadmium
202 reduction and salicylate methods, respectively, during 2009, 2010, and 2012 fieldwork. For
203 samples collected in 2014, nitrate and ammonia were not measured in the field and
204 concentrations were instead determined using ion chromatography (see below). Dissolved O_2 or
205 DO values were determined using Hach® AcuVac Ampuls® with the indigo carmine and the
206 HRDO methods for low and high DO values, respectively, while dissolved sulfide values were
207 measured using the methylene blue method.

208 For fluid samples taken in 2014, concentrations of major anions (F^-, Br^-, Cl^-, SO_4^{-2}, NO_3^-,
209 NO_2^-) and cations (Li^+, Na^+, K^+, Ca^{+2}, Mg^{+2}, NH_4^+) were determined on separate Dionex DX-600
210 ion chromatography (IC) systems using suppressed conductivity detection and operated by
211 Chromeleon software (version 6.8). Samples were stored in high-density polyethylene (HDPE)
212 bottles rinsed and soaked with deionized water. Samples for cations were acidified with 6 N

methanesulfonic acid (MSA) to approximately 19 mM final concentration to suppress carbonate precipitation and ammonia degassing. The anion system employed a potassium hydroxide eluent generator, a carbonate removal device, and AS11-HC/AG11-HC columns. The cation system was equipped with CS-16 and CG-16 columns and cations were eluted isocratically with 19 mM MSA at 0.5 mL/minute. Both systems were plumbed with an external source of deionized water for suppressor regeneration to improve the signal-to-noise ratio of the analyses. Further details on the above method can be found in Fecteau (2016) and Robinson (2018). For 2012 samples, anions and cations were measured using similar methods described in Lindsay et al. (2018). For fluids sampled in 2009 and 2010, anion and cation concentrations were determined using methods described in Canovas et al. (2017). On average, analytical precision for cation and anion analysis was better than 2% and 5% relative standard deviation (RSD), respectively.

An inductively coupled plasma-mass spectrometer (ICP-MS, Thermo Finnigan Element 2™ High Resolution ICP-MS) was used to determine dissolved Al concentrations, and for samples taken in 2014, dissolved Si values, both with precisions mostly within 3% RSD. For samples taken in 2009, 2010, and 2012, dissolved Ca values were determined using both the IC and the ICP-MS (precision mostly within 5% RSD). Generally, both instruments yielded similar values (see Figure S1a) except for a few samples where the IC returned lower concentrations than the ICP-MS. These discrepancies are mostly attributed to fluids sampled during the 2009, 2010, and 2012 fieldwork where IC cation samples were not acidified. Hence, Ca values for all fluids sampled before 2014 are reported using the ICP-MS results. For fluids sampled in 2009, 2010, and 2012, dissolved Si and Mg concentrations were measured using an inductively coupled plasma-optical emission spectrometer (ICP-OES, Thermo iCAP™ 6300). Analytical precision for analysis of Si and Mg was better than 3% and 1% RSD at 1σ, respectively. The Mg

concentrations of a subset of samples from 2012 and 2014 were determined using both the IC and ICP-OES. Both instruments yielded consistent results (see Figure S1b). Reported Mg values for the 2014 samples came from the IC while the rest came from the ICP-OES. For both the ICP-MS and ICP-OES, samples were stored HDPE bottles that were acid-washed and rinsed in deionized water. Before going into the field, bottles were spiked with trace metal grade HNO_3^- to acidify the samples to pH <2. For calibration, a multi-element standard (*High-Purity Standards (HPS),* North Charleston, SC) was used for the ICP-MS while single element standards for Mg and Si (PerkinElmer®, Waltham, MA) were used for the ICP-OES.

Measurements of dissolved inorganic carbon (DIC) concentrations were performed using a wet oxidation total carbon analyzer (OI Analytical 1010 TOC Analyzer) coupled with a Thermo Delta Plus Advantage mass spectrometer. Samples were stored in VWR CS24 amber glass vials with butyl rubber septa, which has low permeability to gases. Each sample was heated followed by acidification with H_3PO_4 to drive off the DIC as CO_2 and analyzed using the mass spectrometer. Further details of the method can be found in Gilles St-Jean (2003) and Robinson (2018). Stable isotope (δ^2H and $\delta^{18}O$) values were determined using an Off Axis - Integrated Cavity Output Spectrometer (OA-ICOS, LGR DLT-100) using methods similar to those reported in Meyer-Dombard et al. (2015). Accounting for instrument drift and normalization to the Vienna Standard Mean Ocean Water (VSMOW) was done following van Geldern and Barth (2012). Precision was usually within ±0.5‰ and ±0.1‰ for δ^2H and $\delta^{18}O$, respectively.

Water isotope analysis was conducted at the Sabo Laboratory at ASU School of Life Sciences. IC and ICP-MS analyses were conducted at the ASU GEOPIG Laboratory while ICP-OES and total carbon analyses where performed at Metals, Environmental and Terrestrial Analytical Laboratory (METAL) at ASU (formerly, ASU Goldwater Environmental Laboratory

and ASU W. M. Keck Foundation Laboratory for Environmental Biogeochemistry). Results of select field and laboratory measurements (pH, temperature, conductivity, water isotope, and dissolved concentrations of major rock-forming elements) are shown in Table 1, while the full dataset is compiled in Table S1.

Results from instrumental analysis were further processed to calculate charge balance, ionic strength, mineral saturation indices, and aqueous speciation with the EQ3/6 program (Wolery and Jarek, 2003) using the thermodynamic dataset described in the supplementary materials. Charge balance and ionic strength of fluids are documented in Table S1, while saturation indices for some minerals are reported in Table S2 in the supplementary files accompanying this work. Results of calculations of aqueous speciation are depicted in Figure S2. Analytical results for circumneutral to slightly alkaline fluids are mostly within 5% of electroneutrality. Results for a few pH <11 well samples have high positive charge imbalance due to unmeasured DIC or, if measured, have unusually low values for this pH range. Unexpectedly low DIC values could be attributed to carbonate precipitation during well sampling or sample storage. Analytical results for hyperalkaline fluids are mostly within 5% of electroneutrality, with some near 20%. At extremes in pH, poor charge balance can be attributed to small uncertainties in pH measurements as OH^- and H^+ are major components of basic and acidic solutions, respectively (*e.g.*, see Nordstrom et al., 2009 for charge imbalance in acidic examples). Shifting field-measured pH values by about 0.1 to 0.2 units, which is within the range of observed fluctuations in the field, results in close to complete charge balance.

Analytical data of most samples from 2010, except for isotopic and dissolved Mg and Si values, were previously reported in the work of Canovas et al. (2017) that focuses on quantifying energy supplies available to chemotrophic microorganisms in serpentinizing fluids. Some fluids

from the 2009, 2010, and 2012 fieldwork were also concomitantly sampled by collaborators (Paukert et al., 2012; 2019). DIC and dissolved Al values determined as described above are reported in Paukert et al. (2012) and repeated here, while concentrations of all other solutes were determined independently. Details on which samples correspond to these previous studies can be found in Table S1. Overall, this work expands analytical data previously reported by the above studies by supplying additional data from 79 fluid samples.

Table 1
Temperature, pH, Conductivity, Water Isotope, and Major Element Compositions of Samples

Sample Number	Site	pH	T	Cond	$\delta^{18}O$	$\delta^{2}H$	DIC	Cl^-	Na^+	K^+	Mg^{+2} (a)	Ca^{+2} (b)	Si^{+4} (c)
			°C	µS/cm	(‰ VSMOW)	(‰ VSMOW)	mmolal	mmolal	mmolal	mmolal	µmolal	mmolal	µmolal
Fluids with pH between 7 to 9													
100112AI	AB	8.5	29	467	3.97	15.35	2.62	1.16	0.81	0.03	1602	0.37	200
140110B	D	8.4	23.5	568	1.49	6.99	3.63	1.58	1.31	0.04	1840	0.49	183
090118P	D	8.8	20.2	973	2.58	13.43	3.68	5.53	4.35	0.10	2148	0.42	169
140114S	F	7.7	21	787	-0.28	3.63	4.39	3.19	3.20	0.11	2010	0.60	200
100107C	M	9.3	25.4	778	-0.86	-0.59	1.93	3.71	3.81	0.09	1445	0.33	289
100107D	M	8.6	25.6	809	-0.81	-1.16	3.08	2.98	3.24	0.07	1522	0.84	347
090120W	M	8.7	24.2	811	-0.70	-3.00	2.83	3.40	3.36	0.09	1691	0.72	397
140111G	Q	8.9	22.6	586	0.25	4.94	4.11	1.53	1.53	0.04	2140	0.36	276
120114O	Q	8.7	23	454	0.62	3.91	2.82	1.30	1.19	0.04	1451	0.30	138
100109X	Q	8.9	23.3	664	-0.34	3.39	4.49	1.71	1.76	0.03	2290	0.40	283
090119S	Q	9.0	21.6	493	1.43	7.80	2.05	2.08	2.03	0.06	1227	0.17	116
090119T	Q	8.6	24.8	527	1.37	6.31	2.78	1.94	1.84	0.05	1541	0.26	239
140116B	SH	7.9	26.5	760	0.33	0.39	5.13	1.28	1.06	0.10	2810	0.56	303
140116C	SH	8.7	27.3	777	0.07	0.35	4.75	1.54	1.37	0.10	2680	0.63	279
120116Q	SH	7.7	25	744	1.07	7.47	5.22	1.28	1.00	0.08	2908	0.51	309
100113AP	SH	7.9	27	723	0.94	4.91	5.17	1.43	1.16	0.08	2680	0.58	288
090123E	SH	8.2	23.9	700	0.93	5.38	4.96	1.37	1.08	0.09	2664	0.51	305
100114AR	SU	8.8	21.5	923	0.14	3.00	3.04	5.19	5.43	0.10	1485	0.45	78.5
090122B	SU	8.8	17.1	1440	0.05	1.54	3.25	9.36	8.90	0.17	1777	0.12	97.2
100115AW	U	8.5	17.5	911	0.26	-1.26	n.d.	7.36	4.51	0.14	314	1.65	33.9
Fluids with pH between 9 and 11													
140110D	D	10.4	21.8	778	0.69	3.73	0.81	4.79	4.92	0.14	782	0.48	91.4
140112L	D	9.8	21.3	659	1.06	6.17	1.88	3.75	3.72	0.11	1150	0.31	111
090118N	D	9.7	17.5	864	1.15	8.10	2.32	6.61	6.22	0.17	1115	0.26	74.6

Table 1 (continued)

100107E	M	10.1	26.9	910	-1.75	-4.63	0.68	4.86	4.89	0.10	885	0.14	214
090120X	M	10.6	27.7	962	-0.98	-4.45	0.15	5.40	5.05	0.12	810	0.95	186
140111H	Q	10.2	20.2	597	0.20	4.46	1.80	3.08	3.59	0.08	1170	0.21	145
140111I	Q	10.9	18.8	683	0.61	6.36	0.85	3.69	4.36	0.10	807	0.37	100
120114N	Q	9.8	21.8	667	-0.32	0.65	2.24	3.17	3.78	0.08	1082	0.28	133
100109T	Q	9.6	23.7	685	-0.19	3.04	3.56	2.38	2.83	0.05	1924	0.04	226
100109W	Q	10.3	20.8	696	0.24	5.83	1.93	3.35	4.15	0.07	1192	0.27	119
090117J	Q	10.6	18.8	823	-0.75	2.41	1.78	4.44	5.16	0.11	994	0.04	104
140116D	SH	9.1	27.1	777	-0.02	0.40	3.98	1.92	1.86	0.10	2430	0.72	260
120116R	SH	10.6	25.8	767	-0.72	1.89	0.76	3.51	4.26	0.12	807	0.19	83.4
100113AN	SH	10.2	28.6	720	-0.27	1.53	1.66	3.32	3.83	0.11	1433	2.17	157
100113AO	SH	10.4	27.4	734	-0.01	2.31	1.40	3.56	4.18	0.11	1298	0.52	138
090123G	SH	10.6	27.6	712	-0.45	1.17	0.59	3.54	3.94	0.12	1535	0.60	176
090122A	SU	10.9	17.4	1215	-0.72	-2.38	0.46	7.83	8.22	0.17	860	0.49	36.3
090122C	SU	10.8	18.5	1154	-1.10	-3.04	0.35	7.95	8.79	0.19	305	1.35	17.8
						Hyperalkaline Spring Fluids (pH >11)							
140115X	AB	11.4	29.5	2949	-0.95	-2.31	0.03	11.4	13.9	0.32	0.45	1.89	2.22
140115Y	AB	11.6	24.5	2778	-0.83	-1.55	0.11	11.8	14.3	0.33	1.26	1.79	2.16
140115Z	AB	11.3	32.2	4050	-0.10	-2.08	0.03	12.6	17.1	0.33	0.41	2.37	1.38
120118Y	AB	11.5	32.5	3343	0.04	-2.47	0.12	6.80	9.24	0.19	1.02	1.88	2.36
120118Z	AB	11.4	30.6	2140	-0.75	-0.70	0.12	9.85	12.1	0.27	0.70	1.50	2.96
120129G	AB	11.0	37.3	1455	-1.50	-4.77	0.05	5.11	5.19	0.15	0.63	1.48	2.82
120129H	AB	11.4	38.2	1616	-1.60	-5.61	0.04	3.41	3.79	0.10	0.51	1.41	2.89
100111AA	AB	11.7	28.5	3400	-0.94	-2.33	0.04	12.0	15.1	0.26	0.28	1.66	1.79
100111AB	AB	11.7	25.4	2770	-1.02	-1.94	0.13	12.3	15.7	0.28	0.79	1.61	2.45
100111AC	AB	11.6	16.5	1873	0.20	3.18	0.69	11.6	14.6	0.29	181	0.33	38.1
100111AD	AB	11.6	32.4	3235	-0.29	-2.64	0.05	13.0	18.1	0.27	0.28	2.18	0.55
100111AE	AB	11.9	18.9	2468	0.03	-0.68	0.07	13.4	18.3	0.29	1.46	0.73	7.84
100111AF	AB	11.9	24.2	2850	-0.74	-1.98	0.10	11.0	15.4	0.22	1.74	1.64	2.49
100112AG	AB	11.1	37.7	1421	-1.24	-3.38	0.04	5.73	6.14	0.15	0.65	1.73	1.37
100112AH	AB	11.2	38.4	1537	-1.72	-4.16	0.05	5.77	6.75	0.14	0.34	1.58	1.43
090116F	AH	11.8	26.3	2250	0.14	4.93	0.11	9.34	11.4	0.31	0.81	1.22	4.28
090116G	AH	11.8	27.1	2230	0.17	3.77	2.80	9.09	11.1	0.27	0.79	1.12	3.35
090116H	AH	11.5	24.5	1890	1.26	9.70	0.57	10.6	13.0	0.28	0.87	0.30	27.8
090116I	AH	11.9	20.7	2200	0.29	6.34	0.18	9.35	11.4	0.27	0.42	0.85	14.7
140110C	D	11.4	27	2011	-0.10	-0.07	0.05	7.45	7.91	0.22	1.30	1.96	4.26
140112K	D	11.4	26.9	1870	-0.77	-2.10	0.04	7.16	7.59	0.21	2.24	1.89	3.88
140112M	D	11.4	28.2	2058	-0.64	-0.45	0.05	7.36	7.89	0.22	0.67	1.98	5.60
090118O	D	11.5	30.3	1905	-0.60	-0.42	0.13	7.56	8.09	0.22	1.82	1.07	11.3
140113O	F	11.4	28.4	2329	-0.52	0.83	0.06	7.92	9.40	0.25	1.07	2.09	3.68
140113P	F	11.5	25.9	2224	-0.54	0.98	0.05	7.90	9.53	0.25	1.28	2.03	1.94
140114R	F	11.6	21.1	1844	-0.72	0.62	0.04	7.10	8.10	0.23	1.46	1.85	2.44

Table 1 (continued)

140114T	F	11.4	27.2	2061	-0.71	1.58	0.04	6.89	7.97	0.22	1.83	1.91	1.84
140114U	F	11.4	21.7	1479	0.24	4.27	0.17	4.72	8.09	0.22	16.1	1.17	7.43
140114V	F	11.4	24.4	1803	-0.21	2.90	0.23	6.98	8.43	0.22	5.60	1.71	2.75
120111A	F	11.6	22.3	1737	-0.07	2.02	0.09	4.62	5.33	0.14	2.04	1.31	7.88
120111B	F	11.4	29.4	1912	-0.41	1.46	0.09	6.39	7.38	0.20	1.32	1.71	4.46
120111C	F	11.3	31.9	1889	-0.45	0.81	0.07	4.94	5.41	0.15	1.07	1.72	6.40
120113I	F	11.4	30	2276	-0.30	0.70	0.14	7.24	8.85	0.22	2.42	1.71	3.29
120113J	F	11.6	25.8	2343	-0.21	1.87	0.09	3.56	4.20	0.10	0.59	1.72	3.82
120113K	F	11.4	30.9	2364	0.72	4.97	0.12	6.10	7.53	0.19	0.45	1.60	20.4
120113L	F	11.3	28.4	2297	1.66	9.71	0.16	10.3	12.79	0.33	0.96	0.73	26.4
100108J	F	11.7	23.9	2214	-0.33	1.91	0.05	8.58	10.4	0.22	1.97	1.89	1.73
100108K	F	11.7	24.7	2266	-0.47	2.00	0.07	8.35	10.4	0.22	1.78	1.87	1.60
100108L	F	11.6	29.2	2442	0.49	4.01	0.07	8.44	10.6	0.22	0.70	1.94	0.89
100108M	F	11.7	26	n.d.	0.27	3.55	0.08	9.99	12.7	0.30	0.46	1.95	7.02
100108N	F	11.6	27.6	2380	-0.05	1.83	0.04	8.28	10.4	0.21	0.89	1.75	0.43
100108O	F	11.8	22	2179	0.16	2.33	0.07	8.70	10.8	0.23	1.12	1.92	0.98
100108P	F	11.5	23.3	1507	0.67	5.48	0.06	7.92	9.61	0.21	15.3	0.56	7.48
100108Q	F	11.6	22.9	1752	0.18	4.44	0.08	7.59	9.19	0.20	6.36	1.19	2.47
100108R	F	11.6	27.9	1967	0.99	3.57	0.06	7.28	8.89	0.18	1.27	1.70	0.78
090115A	F	11.5	29.1	2251	-0.42	0.16	0.10	8.26	9.66	0.25	34.7	2.07	21.9
090115B	F	11.7	24.1	2154	-0.40	0.97	0.12	8.44	9.81	0.27	1.23	1.69	3.68
090115C	F	11.7	25.1	2280	-0.73	0.89	0.06	8.20	9.61	0.25	41.0	2.21	10.6
090115D	F	11.8	20.7	2270	-0.09	2.14	0.16	8.45	9.90	0.26	4.44	1.55	5.13
090115E	F	11.8	18	2240	-0.36	1.00	0.12	8.53	10.0	0.27	1.86	1.70	3.49
100107A	M	11.3	32.4	1900	-2.19	-8.41	0.11	7.25	7.18	0.12	0.21	2.06	37.2
100107B	M	11.3	30.3	1848	-0.92	-5.13	0.11	7.31	7.16	0.14	6.31	1.91	39.3
090120U	M	11.4	31.4	1676	-1.74	-7.86	0.11	7.10	6.58	0.14	102	1.95	50.5
090120V	M	11.4	30.6	1616	-1.68	-8.84	0.05	7.13	6.62	0.16	22.3	1.67	45.0
140111F	Q	11.6	23.8	1470	-0.61	1.07	0.04	4.66	5.86	0.14	3.82	1.69	10.5
120112E	Q	11.3	30.1	1762	-0.56	1.06	0.07	3.38	4.20	0.10	0.68	1.74	5.56
120112F	Q	11.4	27.4	1781	-0.70	0.82	0.11	4.32	5.45	0.13	1.93	1.72	4.62
120112H	Q	11.3	31.9	1893	-0.56	1.41	0.07	4.79	6.33	0.14	0.74	1.80	31.5
100109S	Q	11.8	22.4	1685	-0.37	1.30	0.10	5.32	7.03	0.13	0.54	1.59	3.77
100109U	Q	11.7	24.9	1778	-0.80	0.90	0.12	5.06	6.90	0.11	1.23	1.51	0.47
100109V	Q	11.2	23.7	904	0.41	6.03	0.66	4.25	5.60	0.10	347	0.47	51.7
090117K	Q	11.7	18.5	1074	-0.32	4.18	0.24	5.30	6.60	0.14	74.5	0.25	25.3
090117M	Q	11.7	22.6	1649	-0.62	2.41	n.d.	5.22	6.41	0.15	6.65	1.52	3.82
090119Q	Q	11.7	23.2	1797	-0.52	-0.82	0.13	5.29	6.76	0.15	56.5	1.82	24.0
090119R	Q	11.6	16.6	911	n.d.	n.d.	0.24	5.27	6.89	0.15	10.5	0.20	20.2
140117F	SH	11.5	26.2	1868	-2.04	-6.01	0.03	5.35	6.41	0.15	1.94	1.85	2.65
140117G	SH	11.4	30.5	2015	-2.20	-6.28	0.02	5.33	6.27	0.15	0.79	1.90	1.50
140117H	SH	11.5	29.6	2067	-2.06	-4.91	0.03	5.77	7.14	0.16	1.04	2.08	1.66
140117I	SH	11.3	32.3	2000	-2.22	-5.23	0.05	5.32	6.28	0.15	8.09	1.86	1.96

Table 1 (continued)

140117J	SH	11.3	31.6	1387	-1.79	-4.14	0.07	4.71	5.83	0.14	19.5	0.83	48.9
140117K	SH	11.5	27.4	1980	-2.13	-4.51	0.03	5.76	7.16	0.16	1.48	2.08	2.26
140117L	SH	11.6	27.3	2087	-2.15	-4.33	0.02	5.81	7.33	0.16	1.47	2.14	1.87
120116P	SH	11.2	34.3	1745	-2.10	-4.28	0.06	4.49	5.45	0.13	2.49	1.67	1.70
120116S	SH	11.4	29.5	1729	-1.87	-3.95	0.08	4.58	5.61	0.13	4.54	1.70	2.23
120117T	SH	11.3	32.6	1721	-2.12	-4.06	0.04	3.28	4.01	0.09	1.48	1.65	2.08
120117U	SH	11.3	32	1720	-2.05	-4.19	0.04	5.15	6.25	0.15	0.87	1.65	1.77
120117V	SH	11.7	23.6	1951	-1.67	-2.21	0.08	5.40	6.81	0.14	0.68	1.75	3.63
120117X	SH	11.3	32.8	1681	-2.18	-5.07	0.01	5.10	6.04	0.15	0.56	1.67	2.37
100112AJ	SH	11.5	33.4	1782	-2.22	-5.33	0.05	5.58	7.13	0.12	1.33	1.90	0.59
100112AK	SH	11.5	33.3	1793	-2.63	-5.79	0.04	5.57	7.06	0.12	0.45	1.86	0.73
100112AL	SH	11.5	32.6	1772	-2.45	-5.20	0.04	5.54	7.12	0.12	0.44	1.82	0.57
100112AM	SH	11.5	31.5	1772	-1.97	-4.66	0.04	5.51	7.13	0.12	0.62	1.92	0.53
090123D	SH	11.5	34	1778	-1.93	-4.70	0.09	5.35	6.48	0.15	1.80	1.46	1.91
090123F	SH	11.6	28.1	1770	-1.57	-3.96	0.14	5.61	6.80	0.16	1.86	1.50	1.55
100114AS	SU	11.3	18.2	1013	0.91	0.48	0.47	6.12	7.42	0.14	291	0.30	22.7
100114AT	SU	11.6	30.4	1893	-1.88	-7.27	0.04	6.33	8.40	0.14	0.70	1.72	3.53
100114AU	SU	11.6	20.08	1258	-0.91	-3.64	0.07	6.24	7.80	0.14	157	0.29	16.1
090122Z	SU	11.6	29.5	1897	-2.20	-7.87	0.11	6.01	7.68	0.22	0.54	0.21	4.66
100115AV	U	11.6	21.4	1442	-1.19	-8.79	n.d.	6.99	4.75	0.12	4.15	2.48	0.39
						Well Fluids							
120119B	N14	10.1	24	855	-0.21	-1.71	0.07	4.27	2.31	0.08	32.6	1.14	5.95
120119A	N14	11.1	29.1	1920	0.64	0.89	0.09	7.68	5.40	0.12	5.68	3.42	2.78
120119C	N14	11.0	33.7	2296	0.31	-0.05	0.08	8.12	5.29	0.12	4.19	3.47	2.72
120123E	N04	10.7	28.3	3327	-1.38	-3.65	0.39	7.58	4.05	0.11	10.2	7.73	8.29
120126F	W16	8.0	31.8	492	-0.48	0.11	0.28	0.80	1.17	0.05	1420	0.38	456
120127G	W17	9.2	31	532	-0.56	0.76	2.35	1.16	0.85	0.04	2218	0.05	1.48
120130I	W5	9.3	32.7	595	-0.76	-0.72	1.90	2.03	1.32	0.07	2458	0.05	4.53
120130J	W5	9.4	32.1	610	-0.49	0.21	1.80	2.00	1.31	0.06	2419	0.05	4.42
100119AX	S4B	7.2	33.8	598	-2.54	-10.09	n.d.	1.15	1.26	0.04	1273	1.06	375
100119AY	S4A	7.6	34	491	-3.11	-9.94	n.d.	0.76	0.78	0.04	1123	0.96	366
100120AZ	S3	9.4	34.1	586	-1.00	-4.91	n.d.	2.24	1.58	0.05	2100	0.03	4.38

Notes: b.d.l. - below detection limit; n.d. - not determined; Sites: AB - Al Bana, AL - Al Hilayw, D - Dima, F - Falaij, M - Masibt, Q - Qafifah, SH - Shumayt, SU - Sudari, U - Uqaybah, N14 - NSHQ-14, N04 - NSHQ-04, W16 - WDA-16, W17 - WDA17, W05 - WDA-05, S4A - SJA-04A, S4B - SJA-4B, SJ3 - SJA-03.

[a]All samples were analyzed using the ICP-OES except for those with sample number starting with "14" which were analyzed using the IC.

[b]All samples were analyzed using the ICP-MS, except for these with sample number starting with "14" which were analyzed using the IC.

[c]All samples were analyzed using the ICP-OES except for those with sample number starting with "14" which were analyzed using the ICP-MS.

288

289 **3. Results**

290 3.1. Model Results

291 Model results are described in Leong and Shock (2020) and a worked example is
292 provided in the supplementary files of this paper and illustrated in Figure S4. Specifically,
293 reaction paths depicting various stages of the serpentinization process – primary mineral
294 dissolution (Stage 1), incipient serpentinization (Stage 2), mineral carbonation (Stage 3), brucite
295 formation (Stage 4), H_2 formation (Stage 5), and equilibrium with diopside (Stage 6) – are
296 summarized in the supplementary materials.

297 3.2. Analytical Results

298 Results of field and laboratory analyses are summarized in Figure 3 where samples are
299 classified based on their pH: circumneutral (pH 7 – 9), intermediate (pH 9 – 11), and
300 hyperalkaline (pH >11). Fluids sampled from wells are indicated by the solid black squares
301 regardless of their pH. Samples from Masibt, WDA-16, and fluids from previous studies
302 associated with gabbroic rocks were not included in Figure 3 as simulations on gabbro-water
303 interactions were not conducted in this study. Data from gabbro-hosted fluids are plotted in
304 Figures S7 and S8 and preliminary discussions on their similarities and differences with
305 ultramafic-hosted fluids can be found in the supplementary files accompanying this work.

306 Ultramafic-hosted fluids sampled during this study have pH values ranging from 7.2 to
307 11.9 and conductivities from 450 to 4050 µS/cm. Circumneutral to slightly alkaline fluids are
308 enriched in dissolved O_2 and DIC (Figures 3a and 3b). The dissolved oxygen concentration
309 measured from surface and mixed fluids is constrained by the solubility of atmospheric $O_{2(g)}$,
310 which at ambient conditions (25°C) is close to 275 µmolal. On the other hand, dissolved O_2
311 concentrations of hyperalkaline fluids vary from low concentrations (~10 µmolal) to values close

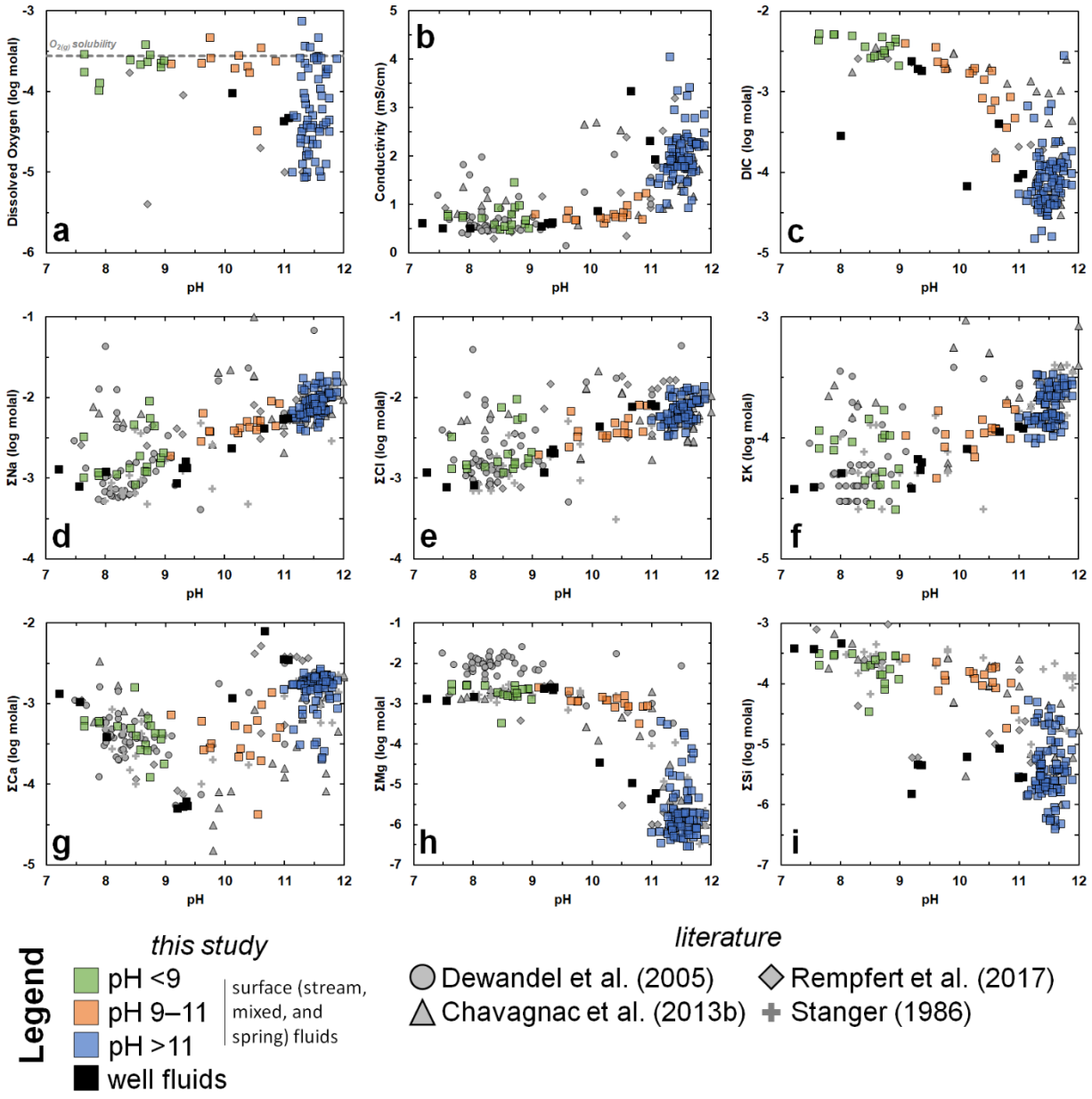

Figure 3. Measured dissolved O_2 (a) and conductivity (b), as well as concentrations of total dissolved inorganic carbon or DIC (c), Na (d), K (e), Cl (f), Ca (g), Mg (h), and Si (i) plotted against pH. Green and blue squares indicate stream and hyperalkaline spring fluids, respectively. Orange squares indicate where fluids resulting from significant mixing between these end-member fluids was physically observed. Black squares show fluids sampled from wells regardless of their pH. Various symbols in grey are values reported in the literature. Dashed grey line in (a) depicts the solubility of O_2 at current atmospheric compositions.

to those measured from circumneutral fluids. This suggests that some of the deep-seated hyperalkaline fluids interact with the atmosphere either during ascent or upon sampling. Hyperalkaline fluids are generally more conductive (Figure 3c) due to elevated total concentrations of Na, Cl, K, and Ca (Figures 3d –3g). Aside from these species, OH^- also contributes to the high conductivities measured in basic solutions. On the other hand, these high-pH fluids are strongly depleted in total dissolved Mg (Figure 3h) and Si (Figure 3i) by approximately 2–3 orders of magnitude relative to circumneutral fluids. Speciation of dissolved solutes are depicted in Figure S2. As shown in Figure S2a, the most common solutes in circumneutral fluids are Mg^{+2} and HCO_3^-. Hyperalkaline fluids are mostly composed of Na^+ and Cl^-, followed by OH^- and Ca^{+2}. As depicted in Figure S2b, most of the dissolved Si in circumneutral fluids exists as $SiO_{2(aq)}$, while the anion $HSiO_3^-$ tends to dominate in hyperalkaline solutions followed by the neutral complex, $NaHSiO_{3(aq)}$. The dominant Mg and Ca species at all pH values of the investigated fluids are Mg^{+2} (Figure S2c) and Ca^{+2} (Figure S2d), respectively. Following Mg^{+2}, the $MgOH^+$ complex can comprise one-third of the total dissolved Mg in hyperalkaline solutions. The dominant DIC component in circumneutral solutions is HCO_3^-, while both CO_3^{-2} and the neutral complex $CaCO_{3(aq)}$ are predominant in hyperalkaline fluids (Figure S2e).

Hyperalkaline fluids sampled from sites close to the basal thrust of the ophiolite (Falaij, Al Bana, Al Hilayw) have higher concentrations, by at most a factor of two, of total dissolved Na, K, and Cl than fluids sampled from other sites (see Figure S3). Results of Mann-Whitney U-test for equal medians show that hyperalkaline fluids sampled from both geological settings are significantly different from each other at $p < 0.01$ (see Table S3 and the supplementary materials for more details on the statistical analysis). We offer possible origins for the elevated

concentrations of Na, Cl, and K of samples collected near the basal thrust in the discussion below. On the other hand, pH and total dissolved Mg, Si, Ca, and inorganic carbon are statistically similar (see Table S3) among high pH samples retrieved from all ultramafic-hosted sites despite their variable geological settings (basal thrust, near or far from the ultramafic-gabbro contact). This suggests similar underlying reactions that constrain these concentrations. We expound further on these reactions in the following section.

Stable isotopic data, $\delta^{18}O$ vs $\delta^{2}H$, of H_2O for fluids sampled in this study are shown in Figure 4, together with relevant local meteoric water lines determined by Weyhenmeyer et al. (2002) for moisture sources coming from the north (Mediterranean, LMWL-N) and the south (Indian Ocean, LMWL-S). Note that fluids hosted in the Samail ophiolite plot between the two meteoric water lines. The Mediterranean Sea is the dominant source of precipitation in modern Oman while the southern moisture source is much rarer and comprised of cyclones and depressions generated in the Indian Ocean that only occasionally reach the northern parts of Oman where the ophiolite is located (Weyhenmeyer et al., 2002). However, Paukert et al. (2019) showed that fluids sampled from the Samail ophiolite are too enriched in ^{18}O and/or depleted in ^{2}H relative to calculated Raleigh distillation curves that model evaporation from the northern Mediterranean source. Our dataset extends that shown by Paukert et al. (2019) and further supports conclusions by previous investigators that fluids hosted in the Samail ophiolite are likely recharged by a combination of northern and southern sources (Weyhenmeyer et al., 2002; Matter et al., 2005; Paukert et al., 2019). Through noble gas geothermometry, Paukert et al. (2019) also showed that some hyperalkaline fluids in Oman were derived from fluids recharged at low temperatures during the last glacial age where the dominant moisture source was likely coming from the south.

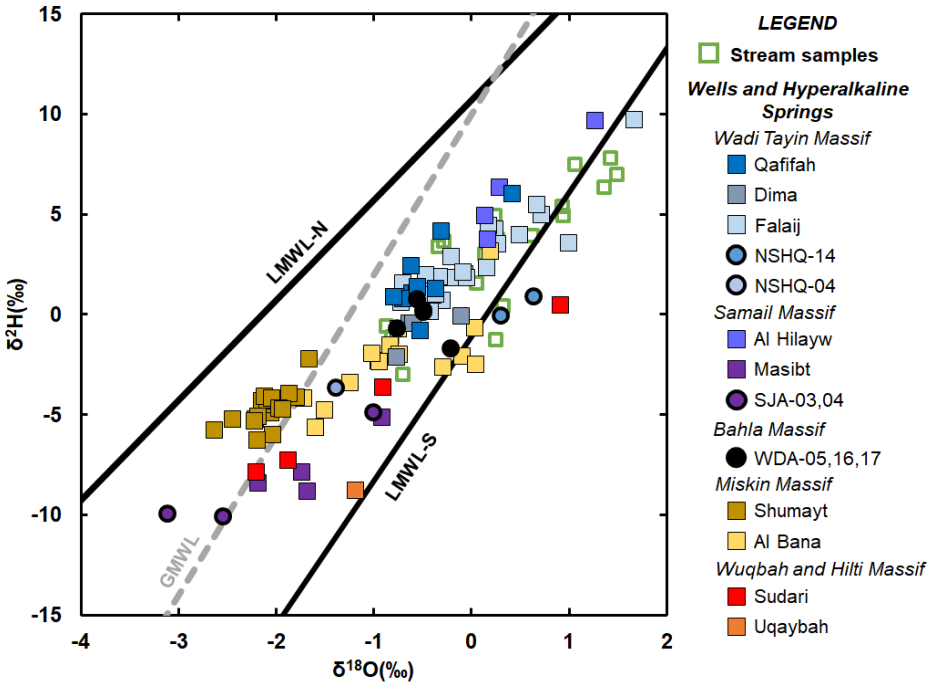

Figure 4. $\delta^{18}O$ vs $\delta^{2}H$ crossplot. Filled circles and squares represent well fluids and hyperalkaline spring fluids, respectively. Colors indicate sample sites of hyperalkaline and well sites (sites in legend are arranged from southeast to northwest in location). Samples in open green squares represents stream samples regardless of location. Local meteoric water lines are plotted based on the southern (LMWL-S) and northern (LMWL-N) moisture sources for Oman (Weyhenmeyer et al., 2002). The grey dashed line depicts the Global Meteoric Water Line (GWML).

Isotopic data from circumneutral to slightly alkaline fluids and hyperalkaline fluids overlap, though some of the latter samples are more depleted in ^{18}O and ^{2}H. In addition, the ^{18}O and ^{2}H compositions of hyperalkaline fluids seem to exhibit geographical trends, that is, fluids from the Miskin Massif (Shumayt and Al Bana) located in the central part of the Samail ophiolite are more depleted in both ^{2}H and ^{18}O relative to those sampled at the Bahla (Wells WDA-05, 16 and 17) and Wadi Tayin (Falaij, Dima, and Qafifah) Massifs, which is further south. Fluids from the northern massifs Wuqbah (Uqaybah) and Hilti (Sudari) and fluids sampled from the northern portions of the Samail Massif (Masibt, and wells SJA-03 and 04) are depleted in ^{2}H relative to the other samples. Fluids sampled from Al Hilayw, located in the southern portion of the Samail

Massif, have isotopic values that plot closely with those from a nearby site from the Wadi Tayin Massif (Falaij). Results of analysis of similarities (ANOSIM) calculations show that many sites have isotopic compositions that are not significantly distinct, though the water isotopic compositions of a given site can be significantly different from another site that is further away (at p <0.05, see Table S4). Results of statistical analyses indicate that samples from Al Bana and Shumayt are the most isotopically unique. However, variabilities in the isotopic compositions from a given study site, especially those trending toward heavier ^{18}O and ^{2}H, can be accounted for by variable degrees of evaporation and can result in compositions that can overlap with those from another study site. Evaporation can thus overprint a much more distinct geographical disparity that can be informed by future isotopic and hydrologic investigations.

4. Reconciling Predictions with Reality

In the following section, compositions measured from environmental samples are compared with those predicted from equilibrium calculations. Deviations from predictions may occur and are likely to be consequences of slower approaches to equilibrium due to kinetic inhibition at low temperatures. Furthermore, several transport processes such as leaching from minerals, the input of infiltrating atmospheric $CO_{2(g)}$, and shallow groundwater mixing with surfacing deep-seated fluids can shift compositions away from those predicted by equilibrium models. We simulate these transport processes, investigate their effect on fluid compositions, and test if these processes can account for natural observations that deviate from equilibrium predictions. We first discuss trends involving pH and dissolved Si, Mg, Ca, and inorganic carbon and then proceed to discuss those for dissolved Na and Cl.

406 4.1. pH and dissolved Si, Mg, Ca, and inorganic carbon

407 Thermodynamic simulations, depicted in Figure S4, predict trends in the dissolved
408 concentrations of Si, Mg, Ca, and inorganic carbon as an outcome in the progress of the
409 subsurface serpentinization reactions. Comparison of predictions with analytical measurements
410 for Si, Mg, Ca, and DIC are shown in pH *vs.* concentration plots in Figures 5a–5d and on activity
411 diagrams representing the MgO-SiO_2-H_2O (Figure 5e) and MgO-CaO-SiO_2-H_2O (Figure 5f)
412 systems. Overall, compositions of fluids measured from environmental samples are generally
413 inconsistent with model results, as most fluid samples do not coincide with predicted reaction
414 paths (solid dark blue curves in Figure 5). Trends from environmental samples show that fluids
415 evolve from relatively dilute rainwater into fluids more concentrated in Si, Mg, and DIC (mainly
416 speciated as HCO_3^-) at pH 7 to 9. Compositions of fluids then evolve into hyperalkaline fluids
417 (pH >11) with low concentrations of Si (Figure 5a) and Mg (Figure 5b). At these highly basic pH
418 values, sampled fluids have high Ca (Figure 5c) and low DIC (Figure 5d) concentrations. The
419 reaction paths generally follow similar trajectories but at different solute concentrations than
420 those measured from the environmental samples. A few environmental samples are consistent
421 with equilibrium predictions. As an example, measured compositions of hyperalkaline fluids
422 seem to be bounded by equilibrium constraints as shown by the end of reaction paths depicted in
423 Figure 5. Specifically, the most depleted Si (Figure 5a) and Mg (Figure 5b) values measured
424 from end-member hyperalkaline fluids in Oman seem to be constrained by equilibrium fluid-
425 mineral reactions (end of the dark blue curves in Figures 5a and 5b), as discussed below. Except
426 for these few cases, most environmental samples cannot be accounted for by equilibrium
427 calculations alone. Hence, we discuss fluid mixing (dashed yellow lines) as a process to account
428 for variations in samples. Compositions of end-member fluids used in our mixing calculations

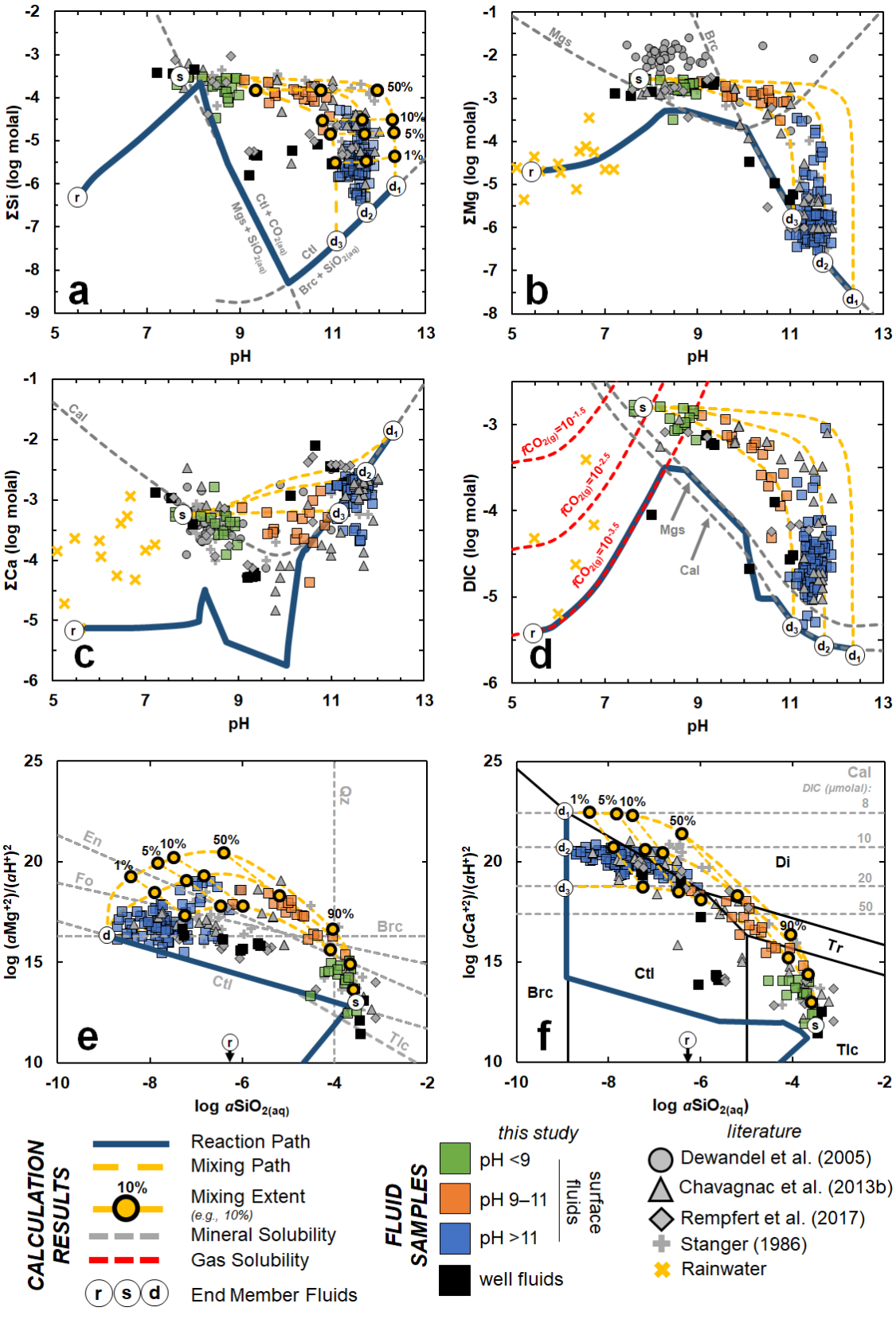
a
ΣSi (log molal)
pH
Ctl + CO2(aq)
Mgs + SiO2(aq)
Ctl
Brc + SiO2(aq)
50%
10%
5%
1%
b
ΣMg (log molal)
Mgs
Brc
c
ΣCa (log molal)
Cal
d
DIC (log molal)
fCO2(g)=10-1.5
fCO2(g)=10-2.5
fCO2(g)=10-3.5
Mgs
Cal
e
log (aMg+2)/(aH+)2
log aSiO2(aq)
En
Fo
Qz
Brc
Ctl
Tlc
90%
f
log (aCa+2)/(aH+)2
Cal
DIC (μmolal):
8
10
20
50
Di
Tr
Brc
Ctl
Tlc
CALCULATION RESULTS
Reaction Path
Mixing Path
Mixing Extent
(e.g., 10%)
Mineral Solubility
Gas Solubility
End Member Fluids
FLUID SAMPLES
this study
pH <9
pH 9–11
pH >11
surface fluids
well fluids
literature
Dewandel et al. (2005)
Chavagnac et al. (2013b)
Rempfert et al. (2017)
Stanger (1986)
Rainwater

429

Figure 5. Comparison of results from reaction path and mineral solubility calculations with total dissolved concentrations of Si (a), Mg (b), Ca (c), and dissolved inorganic carbon (DIC) (d) of samples as well as calculated activities from environmental measurements plotted in activity diagrams for the $MgO\text{-}SiO_2\text{-}H_2O$ (e) and $CaO\text{-}MgO\text{-}SiO_2\text{-}H_2O$ (f) systems at ambient conditions (25°C, 1 bar). Symbols for environmental samples are similar to those in Figure 3, with the addition of rainwater data from Oman and surrounding areas (yellow cross symbols, Ahmed et al., 2000; Matter et al., 2006). Solid dark blue curves represent reaction paths. Dashed grey lines in (a) to (f) show calculated saturation conditions for indicated minerals or mineral assemblages while the solid black lines in (f) depict phase boundaries between minerals. Dashed red lines in (d) depict calculated DIC at indicated $CO_{2(g)}$ fugacity values. Dashed grey line lines in (f) represent calcite saturation at indicated DIC concentrations. Circles with text represent fluids used in the calculations: rainwater (r), representative surface circumneutral fluid (s), representative deep-seated fluids in equilibrium with Ctl-Brc-Di (d_1), Ctl-Brc-Cal at 10 μmolal DIC (d_2), and 20 μmolal DIC (d_3). The latter four compositions (s, d_1, d_2, and d_3) were used as end-member fluids in mixing calculations. Dashed yellow lines represent three mixing paths between these end-member fluids (s and three deep endmembers: d_1, d_2, and d_3) while filled yellow circles along these mixing lines in (a), (e), and (f) represent various mixing extents in %. Upper, middle, and lower dashed yellow curves in (e) indicate mixing between fluid s and fluids d_1, d_2, and d_3, respectively. All three calculated deep-seated fluids (d_1, d_2, and d_3) are coincident in the $MgO\text{-}SiO_2\text{-}H_2O$ activity diagram and are hence just labelled as d in (e). Acronyms for minerals are based on the recommendations of Whitney and Evans (2010): Fo- forsterite, En- enstatite, Ctl- chrysotile, Brc- brucite, Tlc- talc, Qz- quartz, Di- diopside, Cal- calcite.

can be found in Table S6 and details of the calculations are expounded upon below. In addition, we also discuss dissolution of other minerals (*e.g.*, brucite, carbonates) aside from those modeled above (olivine and pyroxene) that can account for some compositional trends observed in natural samples. In the following discussions we first examine pH 7 to 9 fluids enriched in Mg and DIC (green squares) and then proceed to discuss fluids with hyperalkaline (pH >11, blue squares) and intermediate (pH 9 to 11, orange squares) pH. Ultimately, these discussions lead to a classification scheme for these fluid types guided by a combination of constraints from fluid-mineral equilibria and relevant transport processes.

4.1.1. pH 7–9, Mg^{+2}-HCO_3^- Type 1 fluids

Fluids of this type, referred to as Type 1, mainly occur in streams (green squares in Figure 5) and shallow groundwater (some black squares in Figure 5). These fluids are

characterized by neutral to slightly alkaline pH (pH 7–9) and elevated concentrations of DIC, Mg, and Si relative to rainwater and hyperalkaline fluids. As shown in Figure S2a, the most common solutes in these fluids are Mg^{+2} and HCO_3^-, and hence are also referred as Mg^{+2}-HCO_3^- type fluid. In the model, Type 1 compositions are attained at early stages of the overall reaction progress where solutes accumulate in the fluid through initial dissolution of primary minerals but before Si, Mg, and DIC are consumed to form serpentine, carbonates, and brucite. Concentrations of Si in these fluids are consistent with the maximum Si concentrations (Figure 5a) and $a\mathrm{SiO_2}$ (Figure 5e) predicted by the reaction path calculations (black solid curves) when fluids attain equilibrium with serpentine during the start of Stage 2 (see Figure S4d) of the overall reaction progress. As depicted in Figure 5e, environmental samples rarely plot below the chrysotile saturation line, implying constraints on the Si concentrations of ultramafic-hosted fluids by serpentine precipitation. Most of the samples, however, are oversaturated with respect to chrysotile (see Table S2), which implies a kinetic inhibition to serpentine precipitation. Furthermore, most circumneutral to slightly alkaline fluids plot above quartz and talc saturation (see Figure 5e), which suggests kinetic inhibition may apply to most silicates.

While there is close agreement between the equilibrium predictions and the measured Si of Type 1 fluids, the agreement does not hold true for Mg, Ca, and DIC. The modeled concentrations, while showing an increase in these constituents (solid dark blue curves in Figures 5b to 5d), do not increase enough to meet measured concentrations of Mg, Ca, and DIC. Cipolli et al. (2004) showed that these elevated concentrations can be attained during reactions at higher $f\mathrm{CO_2}$, up to two orders of magnitude higher ($f\mathrm{CO_2}$ up to $10^{-1.5}$) than that imposed by the present atmosphere. Results constrained by elevated $f\mathrm{CO_{2(g)}}$ levels are indicated by the reaction paths depicted in Figure 5d as dashed red curves that depict more dissolved $\mathrm{CO_2}$ at higher $f\mathrm{CO_{2(g)}}$

values at a given pH. Alternatively, instead of being the result of elevated $fCO_{2(g)}$, high concentrations of Ca, Mg, and DIC observed in environmental samples in this pH range can also be attained through interactions with minerals that are abundant in serpentinites or highly altered ultramafic rocks that comprise the shallow aquifer. As shown by the dashed grey curves in Figures 5b and 5d, respectively, the lower bounds in the Mg and DIC concentrations of natural fluids with pH values between 7 and 9 are close to those dictated by the solubility of magnesite. In addition, Mg concentrations of Type 1 fluids are between values predicted for fluids in equilibrium with magnesite or brucite (Figure 5b), while the trend in Ca concentrations of the natural samples follows the V-shaped trend of fluids in equilibrium with calcite (Figure 5c). Overall, it can be seen that the compositions of these circumneutral to slightly alkaline fluids are more consistent with the dissolution and precipitation of minerals (serpentine, brucite, magnesite, and calcite) common in the highly altered rocks that compose the shallow aquifer than they are with initial stages of the dissolution of primary minerals in aquifers composed of fresh or relatively less altered ultramafic rocks. This observation is consistent with Neal and Stanger (1986) and Marques et al. (2008), who argued that Mg- and HCO_3^--rich (Type 1) fluids could have been generated in shallow aquifers consisting of highly altered ultramafic rocks. Fluids that plot between the brucite and magnesite solubility curves in Figure 5b can be described by a process involving the dissolution of brucite and subsequent precipitation of magnesite given by,

$$\mathrm{Mg(OH)_{2(brucite)} + Mg^{+2} + 2HCO_3^- \rightarrow 2MgCO_{3(magnesite)} + 2H_2O.} \quad (1)$$

It is possible for reaction (1) to proceed readily at shallow aquifer settings, as brucite is highly soluble at circumneutral pH (see dashed grey curve for brucite in Figure 5b) and is experimentally known to dissolve rapidly at these pH conditions (Pokrovsky and Schott, 2004). Dissolution of brucite likely accounts for the depleted Mg/Si ratios observed from some highly

altered ultramafic rocks relative to those that are less altered (Malvoism, 2015; de Obeso and Kelemen, 2018; 2020), though these observations can likewise be accounted for by enrichment in silica (de Obeso and Kelemen, 2018). It is of note that natural brucite commonly exists in solid solutions of Mg^{+2} and Fe^{+2}, and the dissolution, mobilization, and eventual oxidation of Fe^{+2}-bearing brucite could supply H_2 independent of the H_2 generated during the serpentinization of fresher ultramafic rocks (Frost et al., 2013; Miller et al., 2016; Mayhew et al., 2018; Templeton and Ellison, 2020). However, the production of H_2 from the alteration of brucite-bearing serpentinites can only proceed at O_2-free regions in the aquifer, as Fe^{+2} released from brucite dissolution will be otherwise oxidized by O_2 to form ferric oxyhydroxides.

4.1.2. Hyperalkaline (pH >11) Ca-OH Type 2 fluids

Hyperalkaline fluids were sampled from discharging springs (blue squares in Figure 5) and one well (NSHQ-14). These are classified as Type 2 fluids and are characterized by their hyperalkaline pH, elevated Ca concentrations, and extremely low Si and Mg concentrations. As shown in Figure S2a, the most common solutes in these fluids, after Na^+ and Cl^-, are Ca^{+2} and OH^-, and hence they are also referred to as Ca^{+2}-OH^- fluids. Despite Na^+ and Cl^- comprising most of the total dissolved solutes, these fluids are far less saline than seawater and hence are not often classified as Na^+-Cl^- fluids. Compositions of Type 2 fluids are characteristic of fluids constrained by the chrysotile-brucite-diopside assemblage (Ctl-Brc-Di, see end of reaction path in Figure S4e or reaction S7) predicted by equilibrium calculations. However, upon closer examination, Clt-Brc-Di equilibrium (point d_1 in Figure 5) yields lower Si (Figure 5a) and Mg (Figure 5b) and higher Ca (Figure 5c) concentrations than those measured from environmental samples. Analogous comparisons can be made with the activity diagrams shown in Figures 5e and 5f, where the $a\mathrm{SiO}_{2(aq)}$ values of hyperalkaline samples approach that dictated by Ctl-Brc

equilibrium but plot below the Ctl-Brc-Di equilibrium value. We have yet to sample fluids with Si concentrations or $a\mathrm{SiO}_{2(aq)}$ lower than values dictated by Ctl-Brc equilibrium, implying constraints by this mineral assemblage on the silica content of serpentinization-generated fluids. Despite being close to or approaching predicted compositions, the variabilities in pH and concentrations of dissolved Si and Mg observed for hyperalkaline fluids cannot be fully accounted for by equilibrium predictions. Specifically, pH values of hyperalkaline fluids range from 11 to 12, and at these pH values, Si and Mg concentrations can vary by up to three orders of magnitude. Trends resulting from variabilities in host rock compositions shown by Leong and Shock (2020) cannot account for such wide variations within this small range of pH. Accounting for mineral solid solutions predicts slightly higher Si concentrations (Leong and Shock, 2020) but does not fully reconcile models with actual measurements.

Reaction paths and solubility curves depicted in Figure S4 simulate rainwater-ultramafic rock interactions at 25°C. However, temperatures of fluids during sampling varied from 15° to 40°C. We calculated the pH constrained by the Ctl-Brc-Di equilibrium at temperatures ranging from 0–60°C and results are plotted in Figure 6 (solid black curve). Most environmental samples from Oman, however, have pH values below those predicted by the Ctl-Brc-Di equilibrium. Only a few samples from Oman (grey triangles and x-marks from Chavagnac et al., 2013b and Giampouras et al., 2020, respectively) and a few from other low-temperature serpentinizing environments on Earth (filled black circles in Figure 6) plot near this predicted trend. However, it is of note that pH values higher than those predicted by Ctl-Brc-Di equilibrium are rare, implying that upper limits on the pH of serpentinization-generated fluids are constrained by diopside dissolution. Extremely high pH values (12.5 to >13) were observed in a few continental sites such as in Maqarin, Jordan (Khourey et al., 1985, 1992; Alexander et al., 1992; Pederson et

al., 2004) and Lake Calumet, Chicago (Roadcap et al., 2005; Ohlsson et al., 2019). These localities, however, are not hosted by ultramafic lithologies and the extremely alkaline pH values are likely results of reactions akin to that of groundwater-concrete interactions (Gaucher and Blanc, 2006).

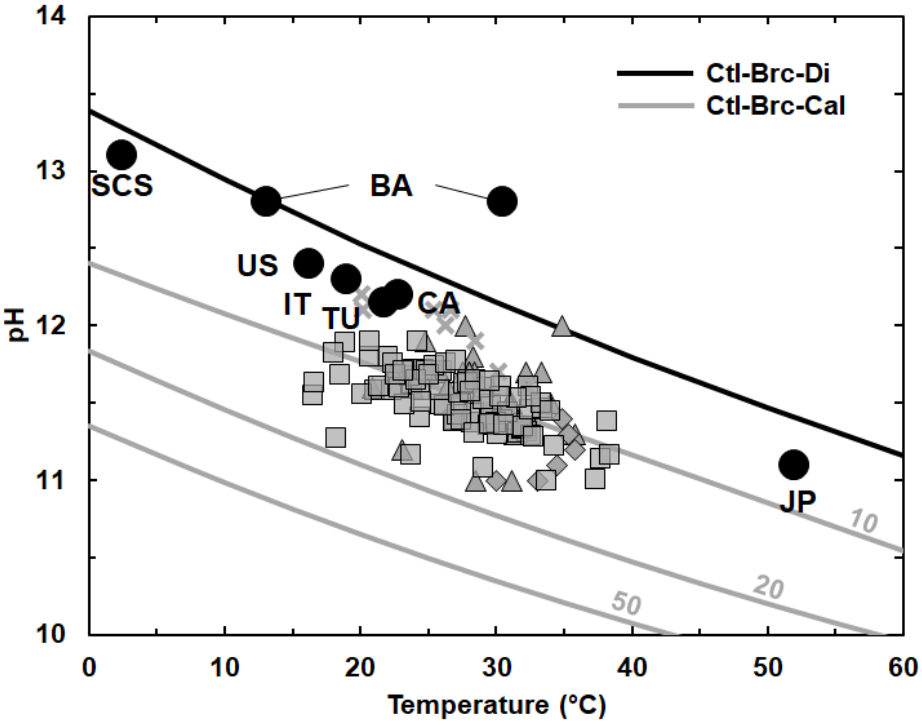

Figure 6. Calculated pH in equilibrium with the Ctl-Brc-Di (solid black curve, reaction 7) and Ctl-Brc-Cal (solid grey curves, reactions 4 and 9) mineral assemblages at temperatures ranging from 0 to 60°C. For the Ctl-Brc-Cal equilibrium assemblages, the DIC concentrations in μmolal are indicated above the solid grey curves. Black circles represent the highest pH values measured in low-temperature serpentinizing systems: SCS- South Chamorro Seamount in the Izu-Bonin-Mariana arc (Mottl, 2009); BA- Dinaride ophiolite in Bosnia and Herzegovina (Etiope et al., 2017); US – Coast Range ophiolites microbial observatory or CROMO, California, USA (Crespo-Medina et al., 2014); CA – Tableland ophiolite, Canada (Szponar et al., 2013); IT – Voltri Massif, Italy (Schwarzenbach et al., 2013); TU – Amik Basin, Turkey (Yuce et al., 2014); and JP – Hakuba Happo spring, Japan (Homma and Tsukahara, 2008; Suda et al., 2014). The pH of these fluids trend closely with and rarely exceed the pH predicted by the Ctl-Brc-Di equilibrium, suggesting that upper limits on the pH of serpentinizing fluids are constrained by diopside dissolution. In contrast, most hyperalkaline (pH >11) fluids from Oman, represented by the various grey symbols, plot below these theoretical maxima but above those predicted for by Ctl-Brc-Cal equilibrium with DIC concentrations of 20 μmolal. Grey square symbols depict data resulting from this work, while those in triangles, diamonds, and crosses represent data reported in Chavagnac et al. (2013b), Rempfert et al. (2017), and Giampouras et al. (2020), respectively.

Leong and Shock (2020) discuss various mineral-fluid reactions (*e.g.*, andradite, calcite) that can shift fluid compositions in equilibrium with Ctl-Brc-Di to lower $a\mathrm{Ca}^{+2}/(a\mathrm{H}^{+})^2$ and hence to lower pH and Ca concentrations. One such process is the introduction of DIC along the fluid pathway, such as when ascending deep-seated hyperalkaline fluids are modified by infiltrating atmospheric $CO_{2(g)}$, mix with DIC-rich shallow groundwaters, and/or come in contact with carbonate veins in the shallow subsurface. Magnesite and dolomite are highly and slightly undersaturated, respectively, in these Mg-poor fluids (see Table S2) and will dissolve upon interaction with surfacing deep-seated fluids. With these additional DIC inputs, Ca-rich hyperalkaline fluids can precipitate calcite, driving fluid compositions away from Ctl-Brc-Di equilibrium to conditions set by chrysotile-brucite-calcite (Ctl-Brc-Cal) equilibrium. The pH values and Ca concentrations constrained by Ctl-Brc-Cal equilibrium vary depending on the amount of DIC supplied by the transport processes mentioned above. Equilibrium with calcite, as shown through the reaction

$$\mathrm{Ca}^{+2} + \mathrm{HCO_3}^{-} \Leftrightarrow \mathrm{CaCO_{3(calcite)}} + \mathrm{H}^{+}, \quad (2)$$

dictates that a higher amount of DIC will result in lower $a\mathrm{Ca}^{+2}/(a\mathrm{H}^{+})^2$. Calculated $a\mathrm{Ca}^{+2}/(a\mathrm{H}^{+})^2$ values at variable DIC concentrations up to 50 μmolal are plotted in the activity diagram shown in Figure 5f. At 25°C and 1 bar, DIC concentrations exceeding 8 μmolal result in $a\mathrm{Ca}^{+2}/(a\mathrm{H}^{+})^2$ values lower than those constrained by Ctl-Brc-Di equilibrium. DIC concentrations of <20 μmolal can account for the $a\mathrm{Ca}^{+2}/(a\mathrm{H}^{+})^2$ of most hyperalkaline samples. Results of calculations of pH constrained by the Ctl-Brc-Cal equilibrium accounting for both variable temperatures (0–60°C) and DIC concentrations (10–50 μmolal) are plotted in Figure 6 (solid grey curves). Most hyperalkaline fluids in Oman have pH values close to those predicted by equilibrium with calcite at DIC concentrations close to 10 μmolal and not more than 20 μmolal, suggesting a DIC-limited

environment in the deep subsurface. Minor DIC input from the atmosphere or through mixing with DIC-rich shallow groundwater can easily saturate calcite and consequently shift the pH of surfacing deep-seated hyperalkaline fluids. Calcite and dolomite were observed in active spring sites in Oman (Kelemen and Matter, 2008) and are evidence that this shift could be actively occurring in the shallow subsurface beneath hyperalkaline discharge zones. Moreover, the extremely low DIC (<20 μmolal) predicted for the subsurface can inform biogeochemical studies on the amount of inorganic carbon available for subsurface microbes. In these carbon-limited environments, dissolution of carbonates can be a robust inorganic carbon source for deep-seated microbes (Miller et al., 2018), and investigations into the subsurface occurrence of these minerals provide insights into how deep the biosphere extends into ultramafic aquifers.

4.1.3. Mixed Fluids

The Si and Mg concentrations of hyperalkaline fluids vary by nearly three orders of magnitude and cannot be fully accounted for by a shift toward Ctl-Brc-Cal equilibrium or by variabilities in temperature. At temperatures between 0–100 °C, predicted total dissolved Si only varies by an order of magnitude and Mg varies even less (Leong and Shock, 2020). Leong and Shock (2020) showed that reaction with more orthopyroxene-rich or more serpentinized ultramafic rocks can lead to higher Si concentrations. However, the same models also predict lower trends in Mg concentrations. Instead, variabilities observed in almost all sampled fluids can be accounted for by mixing (dashed yellow lines in Figure 5) between deep-seated fluids close to equilibrium with the rock as represented by Ctl-Brc-Di (d_1) or Ctl-Brc-Cal (d_2 and d_3) equilibria and a representative surface fluid (s, Sample 140116B). Further details on the composition of end-member fluids used in our mixing calculations can be found in Table S6.

Deep-seated hyperalkaline springs often discharge where neutral to slightly alkaline shallow aquifer fluids discharge as well. Thus, mixing between these two fluid types at discharge zones is likely to occur. As surficial and shallow subsurficial fluids have Si and Mg concentrations that are several orders of magnitude elevated relative to deep-seated hyperalkaline fluids, even minor amounts of mixing can lead to large variabilities in the Si and Mg concentrations. Mixing calculations reveal that a majority of the deep-seated hyperalkaline fluids samples were modified slightly by an input of <10% of surficial and/or shallow surficial fluids (see Figure 5a). Some samples have less influence (<1%) and can be interpreted as the most pristine representatives of the deep subsurface. Using tritium (^{3}H) analysis, Paukert et al. (2019) suggested that hyperalkaline spring fluids in Oman are influenced by up to 6% modern groundwater. This is consistent with our calculated mixing extents for most hyperalkaline fluids (<10%, see Figure 5a).

We use Si concentrations to quantify mixing extents (Figure 5a) because we have constraints on the Si concentration of at least one of the end-member fluids, and it allows us to take advantage of the highly contrasting Si concentrations of end-member fluid types and the generally conservative nature of Si during mixing. In studies involving submarine hydrothermal fluids, the extent of seawater input to venting fluids can be quantified using Na, Cl, and Mg owing to known constraints on end-member concentrations. However, unlike seawater where Na and Cl concentrations are known, end-member Na and Cl concentrations are more variable in continental serpentinizing environments. In the Samail ophiolite, end-member hyperalkaline fluids have Na and Cl concentrations that vary among sample sites, with elevated concentrations observed at sites closest to the basal thrust of the ophiolite. Si behaves more conservatively than Mg, as Mg-bearing minerals such as brucite and layered doubled hydroxides are commonly

observed in hyperalkaline pools (Neal and Stanger, 1984; Paukert et al., 2012; Chavagnac et al., 2013a; Giampouras et al., 2020) and in shallow aquifers (Taylor et al., 1991). Most Type 2 hyperalkaline fluids have $a\mathrm{Mg}^{+2}/(a\mathrm{H}^{+})^{2}$ values that lie above the brucite solubility line, and few cross below it toward the chrysotile saturation line, as shown in Figure 5e.

The Mg *vs* Si concentrations of samples are plotted in Figure S5, along with the calculated mixing pathway depicted in Figure 5. Trends shown in Figure S5 suggest that brucite precipitation at variable pH values above 10, where brucite can be stable or metastable, can cause Mg concentrations to decrease from concentrations along the mixing pathway toward those dictated by the saturation of brucite. In addition, as shown in Figure S5, the Si concentrations of fluids does not decrease to values lower than those depicted along the mixing curves. Despite the thermodynamic drive to precipitate, most fluids remain oversaturated with respect to chrysotile. Tutolo et al. (2018) postulated kinetic inhibition for serpentine precipitation (see reaction S2) or the brucite silicification reaction (see reaction S4), resulting in Si concentrations that are persistently above those dictated by chrysotile solubility (dashed grey lines in Figures 5a and 5e). Mixing can transport Si into a Si-poor deep-seated fluid, and the sluggish rate of serpentine formation makes Si a reliable mixing indicator in comparison to other aqueous species. Though rare, secondary silicate minerals such as suolunite ($Ca_2Si_2O_5(OH)_2{:}H_2O$) are known to precipitate in outcrops (Stanger and Neal, 1984) and hyperalkaline pools (Chavagnac et al., 2013a) in Oman, and determining the rate of Si incorporation into solids at low-temperature conditions will help improve its use as a tracer for mixing in serpentinizing systems. Another advantage of using Si is the ease of measurement of even dilute concentrations (<1 ppm $SiO_{2(aq)}$) in the field using a colorimetric spectrometer. Field measurements can quantify mixing extents during sampling and exploration. Mixing calculations and field measurements of Si concentrations provide a rapid

and robust method to quantify how much the deep-seated signature of serpentinization-generated fluids is affected by shallow subsurface processes.

As a result of mixing, most fluids with pH values greater than 9 have DIC concentrations that imply supersaturation with respect to magnesite and calcite (Figure 5d) and precipitation of these minerals can be favorable. However, at pH >11 calculated DIC levels in equilibrium with magnesite (dashed grey line in Figure 5d) would require Mg values (dashed grey line in Figure 5b) that exceed those measured in our samples, resulting in conditions that are not favorable for precipitation of magnesite (see Table S2). Thus, only calcite (or aragonite, see Table S2) is favored to precipitate in hyperalkaline environments, consistent with studies on travertine and other precipitates associated with hyperalkaline seeps (*e.g.*, Kelemen and Matter, 2008; Chavagnac et al., 2013a; Mervine et al., 2014; Giampouras et al., 2020). At pH values between 9 and 11, Mg (Figure 5b) and DIC (Figure 5d) concentrations of sampled fluids plot above those dictated by magnesite solubility, indicating that magnesite is favored to precipitate in these fluids. Their lack of occurrence in spring sites, however, suggests that there are kinetic inhibitions to precipitate magnesite in surficial mixing environments. These kinetic inhibitions could lead to the precipitation of hydrated magnesium carbonates (*e.g.*, hydromagnesite, dypingite, nesquehonite) that are known to occur in hyperalkaline and mixed fluids in Oman (Giampouras et al., 2020) instead of magnesite. Our mixing calculations also highlight the strong buffering capacity of hyperalkaline fluids resulting from mineral-fluid reactions that generate Ca-OH solutions (Ctl-Brc-Di equilibrium, or Ctl-Brc-Cal equilibrium at low DIC concentrations of <20 μmolal). A significant amount of mixing is required to lower the pH below 11, amounting to 40% surface/shallow water input if pH is constrained by Ctl-Brc-Cal equilibrium at 10 μmolal DIC or up to 80% if constrained to higher pH by Ctl-Brc-Di equilibrium.

690 In addition to fluid mixing, the elevated Si and Mg concentrations relative to those
691 predicted by equilibrium calculations could also result from olivine and pyroxene dissolving
692 faster than serpentine precipitating, as argued by Nesbitt and Bricker (1978). As shown in Figure
693 5e, most hyperalkaline fluids are undersaturated with respect to forsterite and plot between the
694 forsterite and brucite saturation lines. Observations from environmental samples likely reflect
695 complementary primary mineral dissolution and secondary mineral precipitation processes.
696 Quantifying how much the elevated Si and Mg concentrations of hyperalkaline fluids can be
697 attributed to either or both dissolution and mixing processes remains to be solved.

698 4.1.4. pH 9–11, low Si fluids

699 Most samples with pH ranging from 9 to 11 can be attributed to mixing of end-member
700 fluids with the exception of a few samples with dilute Si concentrations (<10 μmolal) that are
701 comparable to those measured in hyperalkaline fluids. These unusually low concentrations of Si
702 at these intermediate pH ranges can be attributed to various processes discussed below.

703 As depicted in Figure 5a, fluids with pH values from 9.0 to 9.5 plot close to the predicted
704 reaction path controlled by equilibria with both chrysotile and magnesite, which signifies fluid
705 compositions indicative of incipient serpentinization (Stage 2) and mineral carbonation (Stage 3)
706 stages of the overall alteration progress. Most fluids of this type were sampled in wells, depicted
707 in Figure 5a as solid black squares (this study) and grey diamonds (Rempfert et al., 2017),
708 suggesting that these fluids could be representative of intermediate stages of the overall
709 serpentinization progress where shallow aquifer fluids are infiltrating into the deep subsurface in
710 the recharge zone. Actual Si concentrations of sampled well fluids could be lower and plot closer
711 to values predicted by equilibrium calculations if upper aquifer fluids, which are Si-rich,
712 contaminate deep-seated samples during sampling of wells.

Alternatively, these fluid compositions could indicate an alteration process involving gabbroic rocks, as many of these fluids were sampled in wells located close to the ultramafic-gabbro contact in the Samail ophiolite. Models simulating water interacting with gabbro or a mixture of gabbroic and ultramafic rocks at low temperatures could assess if these fluids correspond closely with predictions. However, many of the hyperalkaline spring fluids depicted in Figure 5a are also located close to the ultramafic-gabbro transition and do not exhibit any compositional differences from fluids located far from this transition. Like the springs, the composition of these well fluids may be more strongly influenced by fluid-mineral processes associated with ultramafic rocks than with gabbroic rocks.

4.1.5. Classification of ultramafic-hosted fluids

The discussions above provide a framework for classifying low-temperature, ultramafic-hosted fluids as constrained by predictions of the serpentinization reaction path, the solubility of serpentinization-relevant minerals, and the subsequent mixing process that occurs as fluids are discharged back to the surface. Specifically, by drawing on trends in pH and total dissolved Si, as shown in Figure 7, we can classify these fluids into four types (dotted red fields in Figure 7):

Type 1 Mg^{+2}-HCO_3^- – As first proposed by Barnes and O'Neill (1969), these fluids have compositions that are enriched in Mg and bicarbonate, and could be products of the first stage of the alteration progress that leads to enrichment of solutes in fluids through the dissolution of primary minerals in systems open to atmospheric influences (Leong and Shock, 2020). However, as discussed above, these fluids are likely to result from interactions of rain with serpentinites or highly altered ultramafic rocks that are common in the shallow aquifer. Equilibria with serpentine, brucite, and magnesite in the presence of the atmosphere results in fluids with pH values between 7 and 9 that are enriched in Si (~200–500 μmolal, mostly speciated as $SiO_{2(aq)}$),

as depicted in Figure 7. Furthermore, as shown in Figures 5b and 5d, these fluids are enriched relative to other fluid types in Mg (~1000–10,000 μmolal, mostly speciated as Mg^{+2}, see Figure S2c) and DIC (2,000–5,000 μmolal, almost entirely speciated as HCO_3^-, Figure S2e), respectively.

Type 2 Ca^{+2}-OH^- – This fluid type, also first proposed by Barnes and O'Neill (1969), is hyperalkaline and otherwise known as Ca^{+2}-OH^--type fluids. Type 2 fluids are characterized by their high pH (>11), elevated concentrations of Ca (>1,000 μmolal, mostly speciated as Ca^{+2}, Figure S2d), and very low concentrations of Mg and Si (<3 μmolal), which are consequences of equilibria with Ctl-Brc-Di or with Ctl-Brc-Cal at limited DIC concentrations (<20 μmolal) during advanced stages of serpentinization (*Stages 4 to 6*). As shown in Figure 7, a few hyperalkaline samples have Si concentrations that are <3 μmolal (<180 ppb SiO_2) and can be interpreted to be close to end-member Type 2 compositions (<1% mixing). Most other hyperalkaline fluids, however, have higher Si concentrations and can be accounted for by greater degrees of fluid mixing.

Mixed Fluids – In this classification scheme, this fluid type encompasses fluids with pH >9 that are too alkaline to be in equilibrium with serpentine, brucite, and carbonates in the presence of the atmosphere. Note that fluids with pH <9 can also be influenced by mixing, as most fluids sampled in this study plot along the mixing trend shown in Figure 7. At higher pH, this fluid type also includes hyperalkaline fluids that are Si-enriched compared with serpentine + brucite equilibrium. Mixing between circumneutral stream fluids and hyperalkaline springs is commonly observed at the surface, as they often occur together. On the other hand, it is likely that subsurface mixing between end-member Type 1 and 2 fluids in discharge zones accounts for the large variabilities in Si concentration observed in hyperalkaline fluids. The mixing trend

shown in Figure 7 depicts that between end-member Type 1 and 2 fluids. However, mixing can also occur between any fluid type (*e.g.*, between one end-member or mixed fluids with intermediate fluids) that can account for fluids outside the dotted red fields in Figure 7 that represent the four different fluid types discussed in this work.

Intermediate Fluids – These fluids, also with pH values ranging from 9 to 11, share similar characteristics with mixed fluids. However, unlike mixed fluids, these fluids have low Si concentrations (<10 μmolal) that are comparable to most hyperalkaline fluids. As discussed above, fluids of this composition may indicate incipient serpentinization (*Stage 2*) and mineral carbonation (*Stage 3*) during intermediate stages of the alteration progress.

Multivariate statistical analyses (Non-metric Multidimensional Scaling/NMDS and analysis of similarities/ANOSIM) were conducted to evaluate if the overall major element compositions of these four fluid types are significantly different from each other (see supplementary materials for details on statistical methods). Results of NMDS ordination are shown in Figure S6 and depict distinct clustering of circumneutral (Type 1), intermediate, and hyperalkaline (Type 2) fluids. Mixed fluids, especially those with hyperalkaline pH, mostly overlap with end-member Type 2 fluids and indicate that overall compositions of mixed fluids (not just their pH and Si concentrations) are indistinguishable from end-member hyperalkaline solutions. Results of ANOSIM calculations, shown in Table S5, reveal that compositions of intermediate and mixed fluids, despite the overlapping pH, are statistically significant at $p < 0.05$. Mixed and Type 2 fluids, however, are not significantly different at $p < 0.05$. At hyperalkaline conditions, precipitation of brucite and calcite can be fast and drive the Mg and Ca concentrations, respectively, of mixed and Type 2 fluids to values dictated by the saturation curves of these minerals (see Figures 5b and 5c). In addition, ANOSIM results show that the

overall compositions of circumneutral Type 1 and intermediate fluids are not statistically significant at $p < 0.05$ (see Table S5). While the pH and Si concentrations of intermediate fluids are distinct from those of Type 1 fluids, their Mg values are not. As shown in Figure 5b, the Mg concentrations of intermediate fluids (black symbols with pH between 9 and 10) plot close to those dictated by the solubility of brucite. At this pH range, brucite is unstable and dissolution is rapid (Pokrovsky and Schott, 2004), more than 2 and 4 orders of magnitude faster, respectively, than dissolution of olivine (Pokrovsky and Schott, 2000) and chrysotile (Thom et al., 2013). The rapid dissolution of brucite is likely to bring the Mg concentrations of both Type 1 and intermediate fluids to similar values. Both fluid types have the potential to precipitate magnesite, and brucite could have provided additional Mg for mineral carbonation aside from that derived from the primary minerals.

Overall, fluid interaction with both the unaltered and altered aquifer host rocks would result in a diverse composition of fluids that can deviate from equilibrium expectations. However, note that some fluids have Si concentrations that track along the equilibrium reaction path depicting progress of the overall serpentinization reactions, and that the kinetic barriers for precipitation of Si-bearing minerals during mixing (as opposed to brucite and calcite) can provide information on the overall mixing progress. The trends shown in Figure 7 can allow immediate and robust classification of fluids while in the field using a pH meter and a portable spectrometer for colorimetric measurements of dissolved $SiO_{2(aq)}$. These data provide real-time information on the extent of the serpentinization and mixing progress and can concurrently feed into decisions involving exploration, sampling, and experiments while in the field.

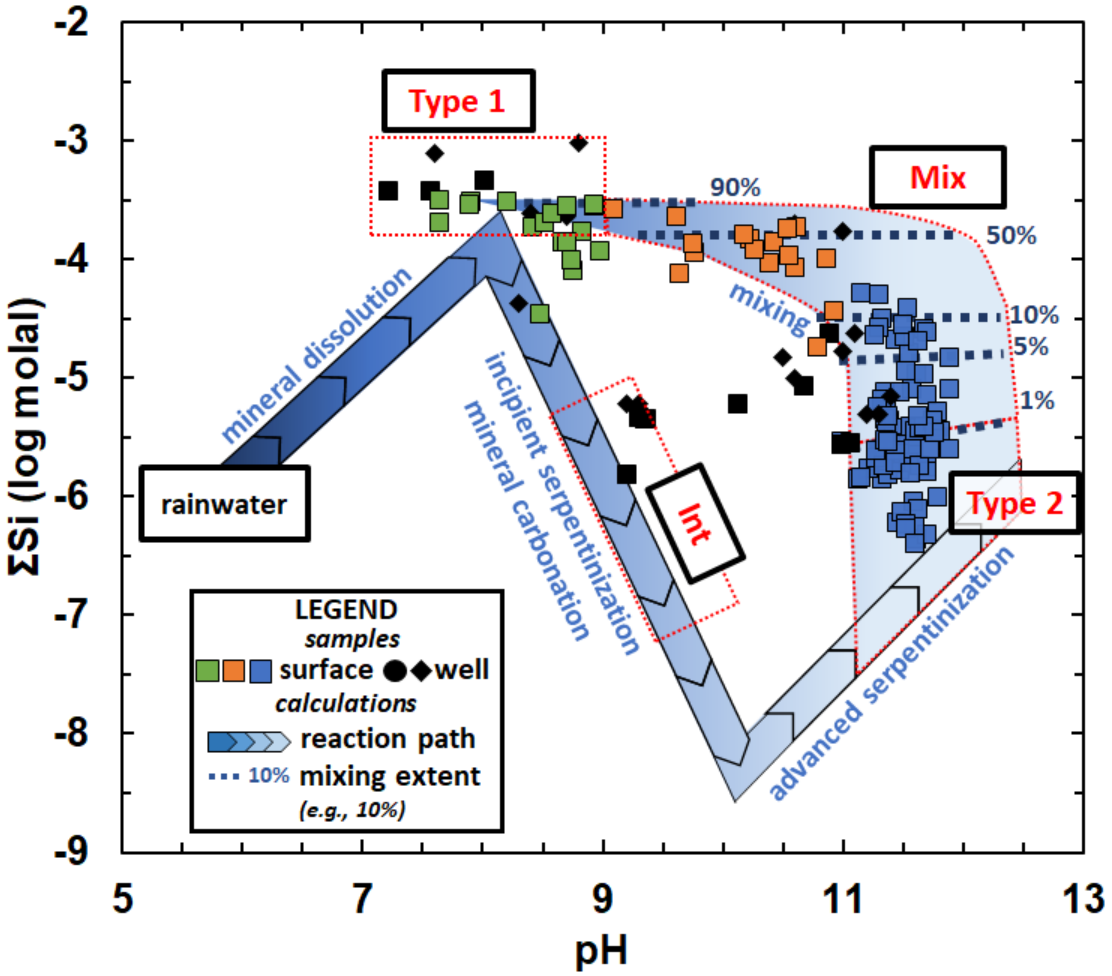

Figure 7. Key serpentinization reactions and resulting fluid types summarized in a plot of Si concentration vs pH. Fluid samples from the Oman ophiolite analyzed in this work (square symbols) as well as well fluids (black diamonds) from Rempfert et al. (2017) are plotted relative to the reaction and mixing paths. Analogous to Figures 3 and 5, colored square symbols depict surface samples where green, orange, and blue symbols represent samples with pH values of <9, between 9 and 11, and >11, respectively. Black squares and diamonds indicate subsurface samples (wells) regardless of their pH. Overall, fluids can be accounted for by four processes: (1) mineral dissolution into rain which leads to Type 1 fluids (see Stage 1), (2) incipient serpentinization and mineral carbonation (see Stages 2–3) which leads to intermediate (Int) fluid types, (3) advanced stages of serpentinization (see Stages 4–6) which lead to Type 2 fluids, and (4) mixing (Mix) between deep-seated Type 2 and surficial or near-surficial Type 1 fluids. Dotted red lines depict suggested pH and dissolved Si values that characterized these four different fluid types. Note that many hyperalkaline fluids (pH >11) are classified as mixed fluids in this scheme.

818 4.2. Dissolved Na and Cl

819 Petrological studies of serpentinized ultramafic rocks reveal that fluid-mobile elements can
820 be sequestered during serpentinization in submarine and subduction environments (Scambelluri
821 et al., 2001; Sharp and Barnes, 2004; Deschamps et al., 2013). The behavior of these elements
822 during serpentinization in continents, where water-rock interactions are facilitated by meteoric
823 fluids instead of seawater, is less well known. Trends in the Na and Cl concentrations of fluids
824 from Oman were investigated to provide insights into their behavior during continental
825 serpentinization.

826 Hyperalkaline fluids are at least twice as enriched in Na (Figure 8a) and Cl (Figure 8b)
827 relative to circumneutral to slightly alkaline fluids and are orders of magnitude enriched relative
828 to rainwater. Similar trends can be observed for K (Figure 3e). The relative enrichment in the Na,
829 K, and Cl content of hyperalkaline fluids can result from two processes: (1) enrichment due to
830 loss of H_2O during the hydration of ultramafic rocks, and/or (2) leaching from host rocks during
831 water-rock interactions. Both can occur concomitantly, as hyperalkaline fluids are products of
832 large extents of water-rock interactions that lead to both water loss and possibly substantial
833 inputs from the reacting rocks. Moreover, the fluids most enriched in Na, K, and Cl are
834 hyperalkaline fluids sampled close to the basal thrust of the Samail ophiolite. These sample
835 locations are typically located at topographic lows which implies longer fluid pathways that lead
836 to more hydration and leaching. Simulations of H_2O loss and leaching were performed to
837 evaluate the influence of hydration and leaching processes in accounting for natural
838 concentrations. The amount of H_2O lost during the overall reaction progress is shown in Figure
839 8c. At log rock-to-water ratio ~0 (*i.e.*, reaction of 1 kg of rock in 1 kg of water), usually inferred
840 as the maximum extent of reactions from deep-sea hydrothermal vent fluids (Taylor, 1974;

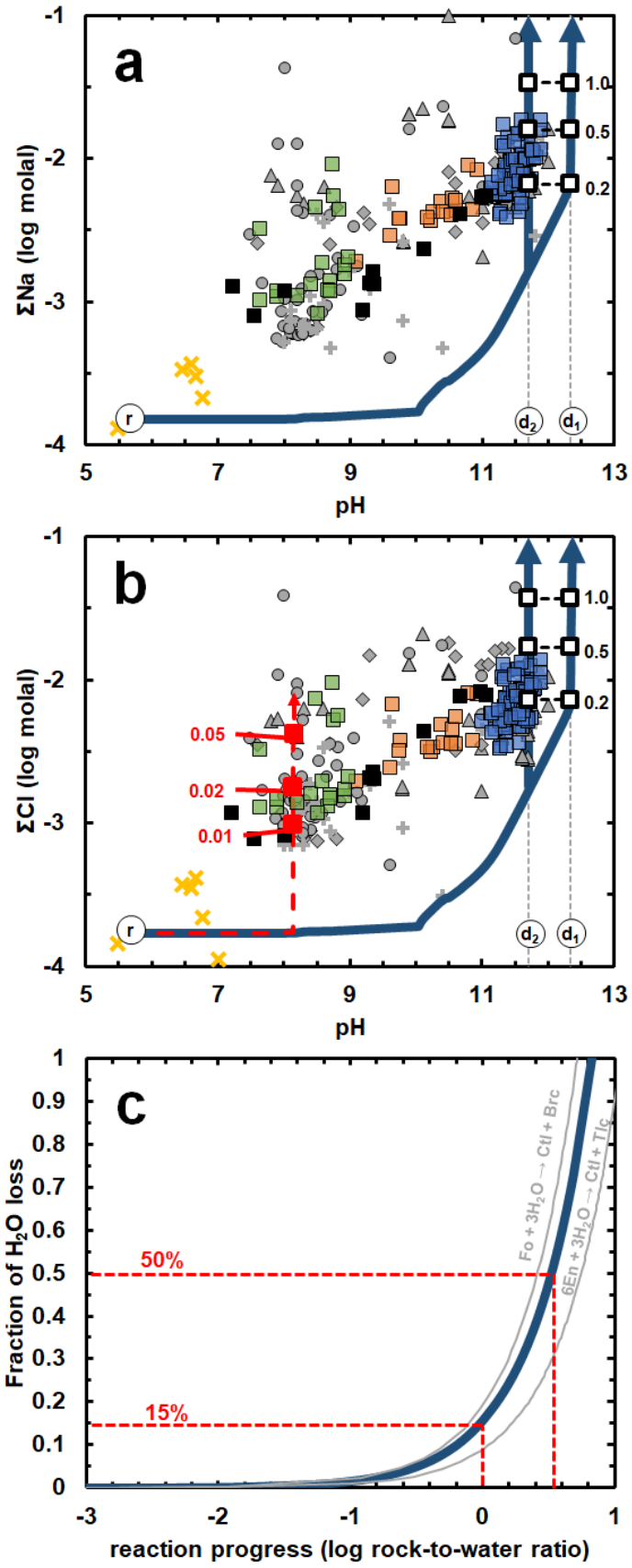
a
ΣNa (log molal)
pH
1.0
0.5
0.2
r
d2
d1
b
ΣCl (log molal)
pH
0.05
0.02
0.01
c
Fraction of H2O loss
reaction progress (log rock-to-water ratio)
50%
15%
Fo + 3H2O → Ctl + Brc
6En + 3H2O → Ctl + Tlc

841

Figure 8. Reaction paths (dark blue curves) depicting predicted trends in the concentration of dissolved Na (a) and Cl (b) due to mineral leaching and amount of H_2O loss (c) as serpentinization progresses. Measured dissolved Na (a) and Cl (b) from environmental samples are plotted for comparison. Symbols in (a) and (b) are the same as those in Figures 3, 5 and 7. Reaction paths start from rainwater (r) and ends at fluids in equilibrium with either the Ctl-Brc-Di (d_1) or the Ctl-Brc-Cal at 10 μmolal DIC (d_2) assemblages. Solid white squares (with bold black outline) indicate extents of water-rock interactions with values of rock-to-water ratios given at the right. The dashed red curve in (b) depicts results of simulations with a serpentinite (100% chrysotile or serpentine). Solid red squares in (b) indicate extents of reactions with values of rock-to-water ratios given at the left. Dark blue curve in (c) represent reaction path for model ultramafic rock with composition 85% olivine-14% orthopyroxene-1% clinopyroxene. Grey curves in (c) represent trends for olivine-only or orthopyroxene-only scenarios. Dashed red lines in (c) show extent of reactions required to remove 15% and 50% of the starting reacting fluid.

Edmond et al., 1979; Foustoukos et al., 2008), the loss of H_2O due to hydration is ~15%. It follows that mineral hydration cannot solely account for the enrichment of Na and Cl observed in sampled fluids. Accounting for an enrichment of at least a factor of two observed from hyperalkaline fluids relative to lower-pH samples requires H_2O loss of >50%, which can only be attained at extremely high rock-to-water ratios (log rock-to-water ratio of >0.5, or reaction of >3 kg of rock in 1 kg of water). Similarly high extents of water-rock interactions are needed regardless of compositional variabilities of the reacting rock (grey curves in Figure 8c). Serpentinization of olivine-rich rocks tend to consume more H_2O as it precipitates more brucite, which contains ~30 wt.% H_2O as hydroxide in its structure. Increased contributions from orthopyroxene favors the formation of serpentine (~13 wt.% H_2O) and talc (~5 wt.% H_2O) which are less hydrous than brucite and would require higher degrees of interaction to result in similar amounts of H_2O loss.

In addition to increases in concentrations due to H_2O loss, Na, K, and Cl can be leached from host rocks during water-rock interactions. Using chemical data from Hanghoj et al. (2010) on the Na content of partially serpentinized Oman harzburgites (~0.03 mole Na^+/kg rock or 0.1 wt.% Na_2O; Cl^- was calculated to balance Na^+ by charge), we can simulate leaching of Na and Cl

during serpentinization. Results of this simulation, depicted as solid dark blue curves in Figures 8a and 8b, show that if Na and Cl were leached from the host rocks during water-rock interactions, it would entail rock-to-water ratios of between 0.2 and 0.5 (*i.e.*, reaction of 0.2 to 0.5 kg of rock in 1 kg of water) to account for environmental measurements. The above range in rock-to-water ratios depicts lower and more plausible extents of water-rock reactions than those required if Na and Cl enrichment is accounted for by mineral hydration only. Neal and Stanger (1985) also postulated in favor of a leaching origin of chloride in hyperalkaline fluids in Oman, as large amounts of H_2O incorporated into serpentine and brucite would result in fluids that are extremely ^{2}H-rich and ^{18}O-depleted. In contrast, as shown in Figure 4, about half of the hyperalkaline fluid analyses (all filled colored symbols in Figure 4), which are indicative of large extents of water-rock interactions, are ^{2}H-depleted relative to circumneutral fluids (open green squares in Figure 4). As for the source of these solutes, Neal and Stanger (1985) indicated that chloride could be leached from mineral surfaces and secondary precipitates such as salts and metal hydroxychlorides. Boschetti and Toscani (2008) also discussed leaching from saline fluid inclusions to account for the elevated concentrations of Na and Cl in hyperalkaline fluids seeping from serpentinite outcrops in Northern Italy. All of the above suggests that the host rocks in these continental aquifers interacted previously with saline fluids, likely during seawater-driven serpentinization before the ophiolite was emplaced onto the continent.

Sodium and chloride concentrations of circumneutral (Type 1) fluids, on the other hand, cannot be accounted for by leaching from rocks with concentrations typical of those from unaltered or partially serpentinized Oman harzburgite, as shown by the solid dark blue curves in Figures 8a and 8b. Since many circumneutral fluids were sampled in surface stream runoffs, evaporation could contribute to enrichment of Na and Cl. However, extreme evaporation of

895 >50% water loss to account for enrichment from typical rainwater concentrations would result in
896 fluids highly enriched in ^{2}H and ^{18}O, which was not observed. Additional input of Na and Cl
897 could have come from interactions with rocks that are more enriched in these elements than
898 typical partially altered ultramafic rocks. The shallow aquifers where these fluids occur are
899 composed of highly altered rocks, which may be more enriched in Na and Cl. We simulated
900 leaching of Cl from serpentinites using the average Cl content (~3000 ppm Cl or 80 millimole
901 Cl/kg rock) of serpentinites or completely serpentinized ultramafic rocks compiled by Deschamp
902 et al. (2013). Results of these calculations, depicted in Figure 8b as the reaction path in dashed
903 red lines, show that only ~7 to 20 grams of serpentinite would need to react with a kilogram of
904 water (log water-to-rock ratio ~-2 to -1.5) to account for the Cl content (0.8-2 millimolal) of
905 most Type 1 fluids. Note that the reaction path shown in Figure 8b depicts reaction of rainwater
906 with a serpentinite and hence the maximum pH at ~8.2 is attained when the rainwater approaches
907 equilibrium with serpentine.

908 Further evidence that supports leaching during the evolution of rainwater into Type 1
909 circumneutral fluids and eventually into Type 2 hyperalkaline fluids is shown in Figure 9a. There
910 is a general increase in the Na/K ratio of fluids as pH increases. The Na/K ratios of all fluid types
911 would remain constant if hydration and evaporation were the only processes accounting for the
912 increasing Na, K, and Cl content. The increasing Na/K ratio with pH could be attributed to
913 leaching from precipitates that formed during previous seawater-rock interactions, as seawater is
914 enriched in Na relative to K.

915 As shown in Figure 9b, the trend in the Na/Cl ratio, like the trend in the Na/K ratio, is not
916 constant with pH. Type 1 fluids (pH <9) are depleted in Na relative to Cl, while Type 2 fluids
917 (pH >11) have Na/Cl ratios above unity or those typical of seawater (0.8). The relative

enrichment of Na with reaction progress could be due to the release of sodium from Na-bearing minerals such as plagioclase and alkali-bearing phyllosilicates (Boschetti and Toscani, 2008; Chavagnac et al., 2013b). Another source could be Na-bearing clinopyroxene, though Chavagnac et al. (2013b) argued that this contribution is likely minor, as these minerals are typically not abundant in harzburgites from Oman. Conversely, another process that could account for the trends shown in Figure 9b is the removal of Cl through incorporation into minerals where structural substitutions for hydroxide are possible, such as in apatite and some phyllosilicates. Layered doubled hydroxides (LDHs) can also attract anions into their positively charged interlayers and are known to occur in hyperalkaline pools and in mixing zones between Type 1 and Type 2 fluids (Paukert et al., 2012; Chavagnac et al., 2013a), as well as in ultramafic-hosted aquifers in Oman (Taylor et al., 1991). Taylor et al. (1991) characterized pyroaurite [$Mg_6Fe^{+3}{}_2(CO_3)(OH)_{16}{:}4H_2O$], the ferric iron end-member of hydrotalcite, from aquifer rocks in Oman that mainly hosts CO_3^{-2} but also contains minor amounts of Cl^- and SO_4^{-2}. These authors proposed that the pyroaurite was generated when Fe^{+2} mobilized during silicate dissolution was partially oxidized during mixing with oxic, shallow fluid sources. Alternatively, Fe-bearing brucite in altered ultramafic rocks could be partially oxidized to form a LDH, as exemplified by the reaction

$$8Mg_{0.75}Fe(II)_{0.25}(OH)_{2(\text{brucite})} + 0.5O_{2(aq)} + 2Cl^- + 3H_2O + 2H^+ \rightarrow Mg_6Fe(III)_2Cl_2(OH)_{16}{:}4H_2O_{(\text{iowaite})} \quad (10)$$

for iowaite, the Cl^- end-member of pyroaurite. Analogous reactions can also be written for other LDHs such as green rust or fougerite, the former of which has numerous properties that are invoked as ideal for the emergence of life on Earth (Russell, 2018). Note that most water samples

retrieved from wells remain chloride-rich (black squares in Figure 9b), implying that alteration processes involving LDHs may be limited to deep-seated fluids surfacing as hyperalkaline seeps.

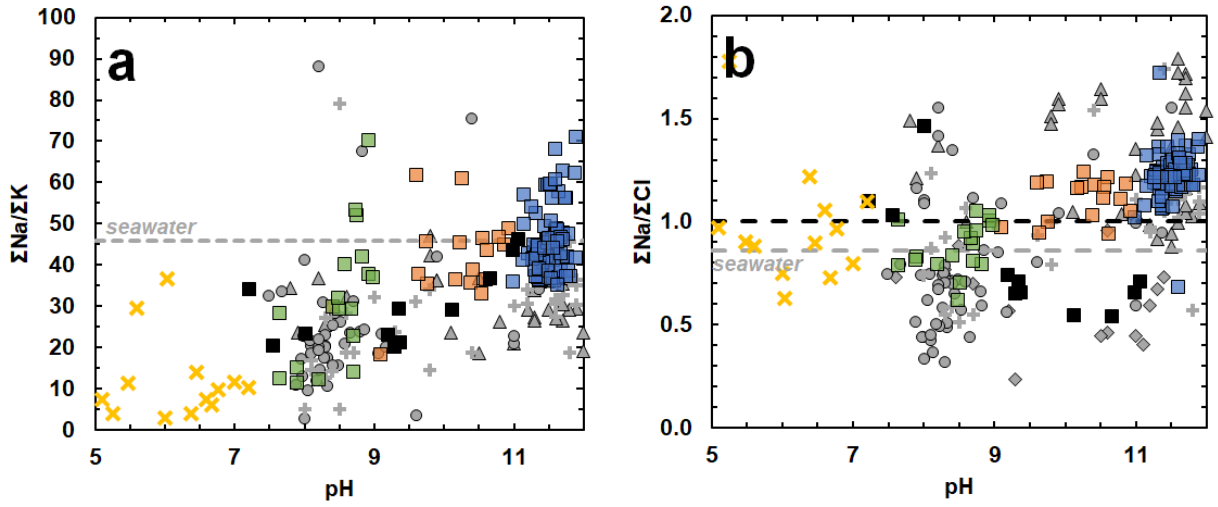

Figure 9. Trends in the total (a) Na/K and (b) Na/Cl ratios of fluids sampled from Oman. Symbols are the same as those in Figures 3, 5, 7, and 8. The increasing Na/K ratio in (a) suggests leaching from host rocks that were altered by seawater-rock interaction. Modern seawater has an average Na/K ratio of ~46 (dashed grey line, Millero et al., 2008). The increasing Na/Cl ratio in (b) suggests additional sources of Na or sinks for Cl. Type 2 fluids have Na/Cl ratios that are above unity (dashed black line) and that typical of seawater (0.86: dashed grey line, Millero et al., 2008).

5. Timescales of Reactions

In the preceding discussions, the extents of water-rock reactions are depicted in terms of rock-to-water ratios that are independent of time. To gain insights into the timescales required to reach the various stages of serpentinization, we conducted reaction path calculations that incorporate dissolution rates of primary minerals at ambient conditions (~25 °C). Rates for forsterite, enstatite, and diopside dissolution are based on experiments of Pokrovsky and Schott (2000), Oelkers and Schott (2001), and Golubev et al. (2005), respectively, which include the pH-dependence of the dissolution rates of the reacting minerals. Calculations were done assuming constant surface area (1 m^2) of fresh ultramafic rock interacting with 1 kg of fluid.

Results are shown in Figure 10a, which depicts both the timescales and the degree of water-rock interactions required to attain the various stages of the overall serpentinization process.

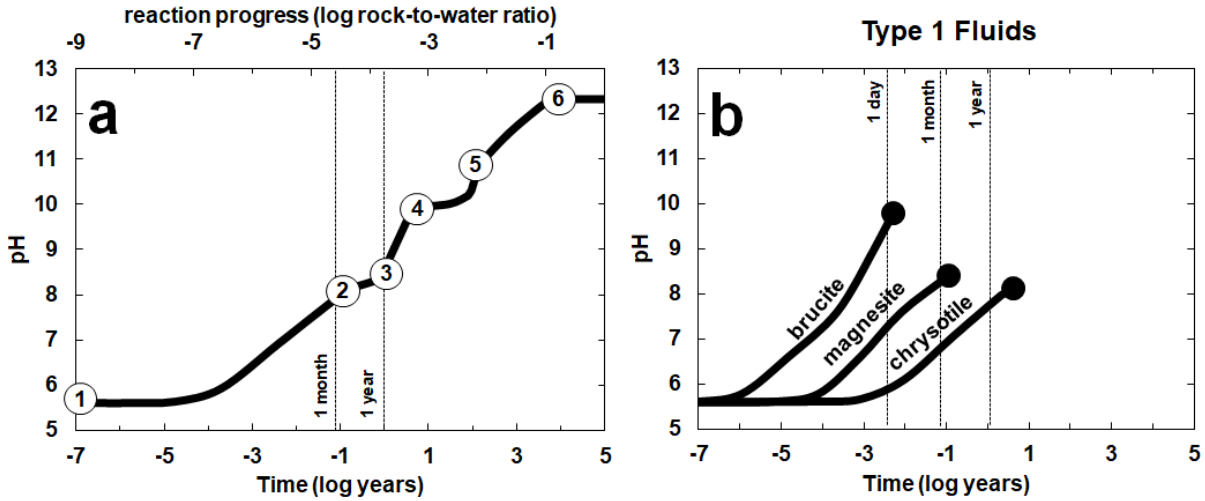

Figure 10. (a) Timescales (in log years) required to attain the various pH and stages of serpentinization. (b) Timescales (in log years) required to attain saturation of three secondary phases common in the altered ultramafic rocks in the shallow subsurface. Numbers inside circles in (a) indicate the starting points of the six stages of serpentinization. Black filled circles in (b) depict end of reaction path depicting dissolution of indicated mineral. Vertical dashed lines indicate various timepoints (1 day, month, and year) as a reference.

Fluids with circumneutral pH (7 to 9) are attained with minimal reaction progress at timescales from a few months to at most a decade. Attaining serpentine saturation (pH ~8, Stage 2) is quick (a few months) while attaining carbonate saturation (Stage 3) entails a few years. However, as discussed above, these circumneutral Type 1 fluids are likely to result from fluid interacting with the highly altered host rocks of shallow aquifers composed mostly of serpentine, brucite, and carbonates. Calculations simulating the dissolution of these secondary phases at ambient conditions were conducted using data from Thom et al. (2013), Pokrovsky and Schott (2004), and Pokrovsky and Schott (1999) for chrysotile, brucite, and magnesite, respectively. The pH-dependences of the dissolution rates were also taken into consideration. Calculations for

977 each of these minerals were done separately and were terminated when fluids reached saturation
978 with the mineral involved. As with the reaction path involving unaltered ultramafic rocks, it is
979 assumed that each kg of water reacts with 1 m^2 surface area of the involved mineral. Although
980 shallow aquifer rocks could be made up of variable proportions of these secondary phases, this
981 idealized assumption allows us to evaluate how rapidly each of these minerals can attain
982 saturation. Results are depicted in Figure 10b, which shows that brucite saturation can be
983 attained relatively quickly owing to its rapid dissolution rates (2 orders of magnitude faster than
984 forsterite dissolution). Fluids would require a few months to attain equilibrium with magnesite.
985 Serpentine saturation can be attained either through the dissolution of primary minerals in
986 ultramafic rocks (Figure 10a, Stage 2) or serpentinites (Figure 10b). Both reach similar fluid
987 chemistry (pH ~ 8) but the latter would require almost a decade, two orders of magnitude slower
988 than the former due to the sluggish dissolution rate of chrysotile relative to those of the primary
989 minerals.

990 Compositions characteristic of Type 2 hyperalkaline fluids (Figure 10a) require much
991 longer durations to attain. As shown in Figure S4, a rock-to-water ratio of at least 0.1 is needed
992 to attain the maximum pH via Ctl-Brc-Di equilibrium (Stage 6), and this requires timescales
993 close to 10,000 years. About 100,000 years would be needed to attain higher extents of reaction
994 at a rock-to-water ratio of 1. Calculated timescales between 10,000–100,000 years correspond to
995 the last glacial age, which is consistent with the hypothesis of Paukert et al. (2019) that some
996 hyperalkaline fluids in Oman were recharged during this period. Our kinetic results also
997 complement the experimental results of McCollom and Donaldson (2016) that show very slow
998 rates of H_2 and CH_4 generation during low-temperature (<100 °C) serpentinization.

Inferred timescales for various stages of serpentinization, however, should be taken cautiously as discrepancies between laboratory-determined dissolution rates and those determined through field studies are well known. Field-determined rates are far slower than those measured in the laboratory, often entailing differences of several orders of magnitude (White and Brantley, 2003). For example, field-determined weathering rates of ultramafic rocks in the Amazon are at least two orders of magnitude more sluggish than laboratory-determined rates (Freyssinet and Farah, 2000). Studies of other lithological settings also report discrepancies between field and laboratory-determined rates (*e.g.*, Velbel, 1993; White and Brantley, 2003; Maher, 2010), with the latter yielding rates at most four orders of magnitude faster than the former. These studies attribute the observed differences to numerous factors such as estimations of reacting surface areas and their evolution during the weathering process, fluid residence times, and the age of the rock. Taking the discrepancies into account, extrapolated timescales from our calculations to natural systems lead to much longer estimates, perhaps even requiring millions of years to attain hyperalkaline conditions if the deviation is at least 2 orders of magnitude. Better constraints on the natural rate at which low-temperature serpentinization occurs would provide powerful insights into the flux of reduced volatiles as well as the rate of energy transfer between the lithosphere and the biosphere in deep ultramafic aquifers here on Earth and other rock bodies in our solar system.

6. Conclusions

Overall, calculations identify the reactions that lead to the contrasting pH, fluid compositions, and redox potentials of end-member Type 1 circumneutral (pH 7 to 9) and Type 2 hyperalkaline (pH >11) fluids. The former are outcomes of mineral dissolution reactions and fluid interactions with highly altered rocks that are common in shallow ultramafic aquifers, while

the latter approach equilibrium with serpentine and brucite, which actively form during advanced stages of serpentinization. The most alkaline fluids documented in low-temperature serpentinizing systems follow constraints dictated by diopside dissolution and some fluids in Oman approach this upper limit. The pH values of most hyperalkaline fluids in Oman, however, are lower than this constraint and can be attributed to a shift from diopside dissolution to calcite precipitation driven by the addition of dissolved inorganic carbon (DIC) as surfacing deep-seated hyperalkaline fluids encounter the atmosphere.

Most fluids with pH values between those of Type 1 and Type 2 can be attributed to mixing of these end-member fluids. Our calculations highlight potential imprints of *shallow* subsurficial processes on the deep-seated signatures of discharging hyperalkaline fluids through mixing. Shallow portions of the *discharge* zone could be hotspots for subsurface life that may bloom where reduced deep-seated fluids encounter oxidized shallow aquifer fluids. As systems with contrasting oxidation-reduction potentials meet, habitability is defined by the extent to which such systems fail to equilibrate abiotically, leaving opportunities for microbial communities to exploit.

In contrast, some fluids with pH values between 9 and 11 do not correspond to mixing trends between end-member fluids. Rather than forming through mixing, these fluids may be indicative of intermediate stages of serpentinization. As this stage of reaction progress corresponds to incipient serpentinization and the carbonation of ultramafic rocks, further focus on this fluid type could help inform potential studies targeting ultramafic aquifers as hosts for deep storage of sequestered atmospheric CO_2 (Kelemen and Matter, 2008; Kelemen et al., 2011; National Academies, 2019). In addition, targeting fluids with these compositions will also reveal information on reactions that facilitate the transformation of oxic surface fluids into reduced,

deep-seated, hyperalkaline fluids as they infiltrate deeper into the aquifer. Conditions for habitable environments may exist through this fluid transformation and future exploration of this fluid type will provide insights into the habitability of *recharge* zones of the fluid pathway and how they differ from *discharge* zones and their surface expressions. The Oman Drilling Project (omandrilling.ac.uk, Kelemen et al., 2013) recently drilled several wells that tap into fluids indicative of various stages of serpentinization and is poised to reveal a comprehensive assessment of microbial communities powered by rock and fluid interactions in the ultramafic subsurface. Models from this work can be used to assess these samples. We also propose the practicality of measuring both pH and Si concentrations with field-portable equipment, allowing rapid assessment of fluid type and extents of mixing while in the field, which can augment exploration with real-time information.

We demonstrated that the compositions of serpentinization-generated fluids can be partly accounted for by predictions of fluid-mineral equilibria and showed how processes such as leaching and fluid mixing can account for compositions that deviate from equilibrium expectations. Both water and ultramafic rocks are believed to abound in ice-covered ocean worlds in our Solar System such as Europa and Enceladus, and serpentinization is thought to enable habitable environments in these terrestrial bodies as it does on Earth (Vance et al., 2007; Holms et al., 2015; Glein et al., 2015; Waite et al., 2017; Glein and Zolotov, 2020). By demonstrating that simulations of low-temperature serpentinization can be successfully applied to analogous processes here on Earth, this work substantiates these calculations as useful tools in exploring serpentinization reactions beyond our own planet.

Finally, further work on the kinetics of low-temperature serpentinization, whether determined through laboratory experiments or in the field, will ultimately provide stronger

constraints on the rate of energy transfer between the lithosphere and the subsurface biosphere. Rates will also feed into reactive transport simulations that could improve upon the calculations described here and reveal how various transport processes contribute to the overall compositions of serpentinization-generated fluids.

7. Acknowledgments

Samples used in this study were gathered with the help of Peter Kelemen, Juerg Matter, Amelia Paukert Vankeuren, Lisa Streit, Peter Canovas, Jeff Havig, and Peter Marsala. We also would like to thank Tracy Lund, Natasha Zolotova and Roy Erikson for help in analysis of fluid samples at the ASU GEOPIG laboratory, W.M. Keck Foundation Laboratory for Environmental Biogeochemistry, and Goldwater Environmental Laboratory (the latter two now merged as the Metals, Environmental and Terrestrial Analytical Laboratory (METAL)). Thanks also to Tucker Ely, Vincent Milesi, and Grayson Boyer for helpful discussions on computational tools used in this study. This work was supported by NASA Exobiology grant NNX12AB38G, the NASA Astrobiology Institute Rock-Powered Life (RPL) and Exploring Ocean Worlds (ExOW) projects, and NSF grant EAR-1515513. By acceptance, all analytical and theoretical results (Tables S1 and S2) will be stored and uploaded at the EarthChem Library portal.

8. References

Ahmed, A. F. M., Singh, R. P., & Elmubarak, A. H. (1990). Chemistry of atmospheric precipitation at the Western Arabian Gulf Coast. *Atmospheric Environment. Part A. General Topics*, *24*(12), 2927–2934. https://doi.org/10.1016/0960-1686(90)90473-Z

Alexander, W. R., Dayal, R., Eagleson, K., Eikenberg, J., Hamilton, E., Linklater, C. M., McKinley, I. G., & Tweed, C. J. (1992). A natural analogue of high pH cement pore waters from the Maqarin area of northern Jordan. II: results of predictive geochemical

calculations. *Journal of Geochemical Exploration*, *46*(1), 133–146. https://doi.org/10.1016/0375-6742(92)90104-G

Amend, J. P., McCollom, T. M., Hentscher, M., & Bach, W. (2011). Catabolic and anabolic energy for chemolithoautotrophs in deep-sea hydrothermal systems hosted in different rock types. *Geochimica et Cosmochimica Acta*, *75*(19), 5736–5748. https://doi.org/10.1016/j.gca.2011.07.041

Barnes, I., O'Neil, J. R., & Trescases, J. J. (1978). Present day serpentinization in New Caledonia, Oman and Yugoslavia. *Geochimica et Cosmochimica Acta*, *42*(1), 144–145. https://doi.org/10.1016/0016-7037(78)90225-9

Bath, A., Christofi, N., Neal, C., Philp, J., Cave, M., McKinley, I., & Berner, U. (1987). *Trace element and microbiological studies of alkaline groundwaters in Oman, Arabian Gulf: a natural analogue for cement pore-waters*. British Geological Survey, Fluid Processes Research Group.

Boschetti, T., & Toscani, L. (2008). Springs and streams of the Taro–Ceno Valleys (Northern Apennine, Italy): Reaction path modeling of waters interacting with serpentinized ultramafic rocks. *Chemical Geology*, *257*(1), 76–91. https://doi.org/10.1016/j.chemgeo.2008.08.017

Boulart, C., Chavagnac, V., Monnin, C., Delacour, A., Ceuleneer, G., & Hoareau, G. (2013). Differences in gas venting from ultramafic-hosted warm springs: The example of Iman and Voltri Ophiolites. *Ofioliti*, *38*(2), 142–156. https://doi.org/10.4454/ofioliti.v38i2.423

Boyd, E. S., Amenabar, M. J., Poudel, S., & Templeton, A. S. (2020). Bioenergetic constraints on the origin of autotrophic metabolism. *Philosophical Transactions of the Royal Society A: Mathematical, Physical and Engineering Sciences*, *378*(2165), 20190151.

https://doi.org/10.1098/rsta.2019.0151

Bruni, J., Canepa, M., Chiodini, G., Cioni, R., Cipolli, F., Longinelli, A., Marini, L., Ottonello, G., & Vetuschi Zuccolini, M. (2002). Irreversible water–rock mass transfer accompanying the generation of the neutral, Mg–HCO_3 and high-pH, Ca–OH spring waters of the Genova province, Italy. *Applied Geochemistry, 17*(4), 455–474. https://doi.org/10.1016/S0883-2927(01)00113-5

Canovas, P. A., Hoehler, T., & Shock, E. L. (2017). Geochemical bioenergetics during low-temperature serpentinization: An example from the Samail ophiolite, Sultanate of Oman. *Journal of Geophysical Research: Biogeosciences*, *122*(7), 1821–1847. https://doi.org/10.1002/2017JG003825

Charlou, J. L., Donval, J. P., Fouquet, Y., Jean-Baptiste, P., & Holm, N. (2002). Geochemistry of high H2 and CH4 vent fluids issuing from ultramafic rocks at the Rainbow hydrothermal field (36°14′N, MAR). *Chemical Geology, 191*(4), 345–359. https://doi.org/10.1016/S0009-2541(02)00134-1

Chavagnac, V., Ceuleneer, G., Monnin, C., Lansac, B., Hoareau, G., & Boulart, C. (2013a). Mineralogical assemblages forming at hyperalkaline warm springs hosted on ultramafic rocks: A case study of Oman and Ligurian ophiolites: Mineral Precipitate at Alkaline Springs. *Geochemistry, Geophysics, Geosystems*, *14*(7), 2474–2495. https://doi.org/10.1002/ggge.20146

Chavagnac, V., Monnin, C., Ceuleneer, G., Boulart, C., & Hoareau, G. (2013b). Characterization of hyperalkaline fluids produced by low-temperature serpentinization of mantle peridotites in the Oman and Ligurian ophiolites: Hyperalkaline Waters in Oman and Liguria. *Geochemistry, Geophysics, Geosystems*, *14*(7), 2496–2522.

https://doi.org/10.1002/ggge.20147

Cipolli, F., Gambardella, B., Marini, L., Ottonello, G., & Vetuschi Zuccolini, M. (2004). Geochemistry of high-pH waters from serpentinites of the Gruppo di Voltri (Genova, Italy) and reaction path modeling of CO_2 sequestration in serpentinite aquifers. *Applied Geochemistry*, *19*(5), 787–802. https://doi.org/10.1016/j.apgeochem.2003.10.007

Crespo-Medina, M., Twing, K. I., Kubo, M. D. Y., Hoehler, T. M., Cardace, D., McCollom, T., & Schrenk, M. O. (2014). Insights into environmental controls on microbial communities in a continental serpentinite aquifer using a microcosm-based approach. *Frontiers in Microbiology*, *5*, no. 604. https://doi.org/10.3389/fmicb.2014.00604

Deschamps, F., Godard, M., Guillot, S., & Hattori, K. (2013). Geochemistry of subduction zone serpentinites: A review. *Lithos*, *178*, 96–127. https://doi.org/10.1016/j.lithos.2013.05.019

Dewandel, B., Lachassagne, P., Boudier, F., Al-Hattali, S., Ladouche, B., Pinault, J.-L., & Al-Suleimani, Z. (2005). A conceptual hydrogeological model of ophiolite hard-rock aquifers in Oman based on a multiscale and a multidisciplinary approach. *Hydrogeology Journal*, *13*(5–6), 708–726. https://doi.org/10.1007/s10040-005-0449-2

Edmond, J. M., Measures, C., McDuff, R. E., Chan, L. H., Collier, R., Grant, B., Gordon, L. I., & Corliss, J. B. (1979). Ridge crest hydrothermal activity and the balances of the major and minor elements in the ocean: The Galapagos data. *Earth and Planetary Science Letters*, *46*(1), 1–18. https://doi.org/10.1016/0012-821X(79)90061-X

Etiope, G., & Whiticar, M. J. (2019). Abiotic methane in continental ultramafic rock systems: Towards a genetic model. *Applied Geochemistry*, *102*, 139–152. https://doi.org/10.1016/j.apgeochem.2019.01.012

Etiope, G., Samardžić, N., Grassa, F., Hrvatović, H., Miošić, N., & Skopljak, F. (2017). Methane

and hydrogen in hyperalkaline groundwaters of the serpentinized Dinaride ophiolite belt, Bosnia and Herzegovina. *Applied Geochemistry*, *84*, 286–296. https://doi.org/10.1016/j.apgeochem.2017.07.006

Fecteau, K. M. (2016). *Organic Carbon in Hydrothermal Systems: from Phototrophy to Aldehyde Transformations*. Arizona State University.

Fones, E. M., Colman, D. R., Kraus, E. A., Nothaft, D. B., Poudel, S., Rempfert, K. R., Spear, J. R., Templeton, A. S., & Boyd, E. S. (2019). Physiological adaptations to serpentinization in the Samail Ophiolite, Oman. *The ISME Journal*, *13*(7), 1750–1762. https://doi.org/10.1038/s41396-019-0391-2

Foustoukos, D. I., Savov, I. P., & Janecky, D. R. (2008). Chemical and isotopic constraints on water/rock interactions at the Lost City hydrothermal field, 30°N Mid-Atlantic Ridge. *Geochimica et Cosmochimica Acta*, *72*(22), 5457–5474. https://doi.org/10.1016/j.gca.2008.07.035

Freyssinet, P., & Farah, A. S. (2000). Geochemical mass balance and weathering rates of ultramafic schists in Amazonia. *Chemical Geology*, *170*(1), 133–151. https://doi.org/10.1016/S0009-2541(99)00245-4

Frost, B. R., Evans, K. A., Swapp, S. M., Beard, J. S., & Mothersole, F. E. (2013). The process of serpentinization in dunite from New Caledonia. *Lithos*, *178*, 24–39. https://doi.org/10.1016/j.lithos.2013.02.002

Früh-Green, G. L., Orcutt, B. N., Rouméjon, S., Lilley, M. D., Morono, Y., Cotterill, C., Green, S., Escartin, J., John, B. E., McCaig, A. M., Cannat, M., Ménez, B., Schwarzenbach, E. M., Williams, M. J., Morgan, S., Lang, S. Q., Schrenk, M. O., Brazelton, W. J., Akizawa, N., Boschi, C., Dunkel, K. G., Quéméneur, M., Whattam, S. A., Mayhew, L., Harris, M.,

1183 Bayrakci, G., Behrmann, J.-H., Herrero-Bervera, E. Hesse, K., Liu, H.-Q., Ratnayake, A.
1184 S., Twing, K., Weis, D., Zhao, R., & Bilenker, L. (2018). Magmatism, serpentinization
1185 and life: Insights through drilling the Atlantis Massif (IODP Expedition 357). *Lithos*,
1186 *323*, 137–155. https://doi.org/10.1016/j.lithos.2018.09.012
1187 Gaucher, E. C., & Blanc, P. (2006). Cement/clay interactions – A review: Experiments, natural
1188 analogues, and modeling. *Waste Management*, *26*(7), 776–788.
1189 https://doi.org/10.1016/j.wasman.2006.01.027
1190 Geldern, R. van, & Barth, J. A. C. (2012). Optimization of instrument setup and post-run
1191 corrections for oxygen and hydrogen stable isotope measurements of water by isotope
1192 ratio infrared spectroscopy (IRIS). *Limnology and Oceanography: Methods*, *10*(12),
1193 1024–1036. https://doi.org/10.4319/lom.2012.10.1024
1194 Giampouras, M., Garrido, C. J., Bach, W., Los, C., Fussmann, D., Monien, P., & García-Ruiz, J.
1195 M. (2020). On the controls of mineral assemblages and textures in alkaline springs,
1196 Samail Ophiolite, Oman. *Chemical Geology*, *533*, no. 119435.
1197 https://doi.org/10.1016/j.chemgeo.2019.119435
1198 Glein, C. R., Baross, J. A., & Waite, J. H. (2015). The pH of Enceladus' ocean. *Geochimica et*
1199 *Cosmochimica Acta*, *162*, 202–219. https://doi.org/10.1016/j.gca.2015.04.017
1200 Glein, C. R., & Zolotov, M. Y. (2020). Hydrogen, hydrocarbons, and habitability across the solar
1201 system. *Elements*, *16*(1), 47–52. https://doi.org/10.2138/gselements.16.1.47
1202 Golubev, S. V., Pokrovsky, O. S., & Schott, J. (2005). Experimental determination of the effect
1203 of dissolved CO_2 on the dissolution kinetics of Mg and Ca silicates at 25 °C. *Chemical*
1204 *Geology*, *217*(3), 227–238. https://doi.org/10.1016/j.chemgeo.2004.12.011
1205 Hammer, O., Harper, D. A. T., & Ryan, P. D. (2001). PAST: Paleontological statistics software

package for education and data analysis. *Palaeontologia Electronica*, *4*(1), 9pp.

Hanghøj, K., Kelemen, P. B., Hassler, D., & Godard, M. (2010). Composition and genesis of depleted mantle peridotites from the Wadi Tayin Massif, Oman Ophiolite; Major and trace element geochemistry, and Os isotope and PGE systematics. *Journal of Petrology*, *51*(1–2), 201–227. https://doi.org/10.1093/petrology/egp077

Helgeson, H. C., Delaney, J. M., Nesbitt, H. W., & Bird, D. K. (1978). Summary and critique of the thermodynamic properties of rock-forming minerals. *American Journal of Science*, *278*, 1–229.

Holm, N. G., Dumont, M., Ivarsson, M., & Konn, C. (2006). Alkaline fluid circulation in ultramafic rocks and formation of nucleotide constituents: A hypothesis. *Geochemical Transactions*, *7*(1), no. 7. https://doi.org/10.1186/1467-4866-7-7

Holm, N. G., Oze, C., Mousis, O., Waite, J. H., & Guilbert-Lepoutre, A. (2015). Serpentinization and the formation of H_2 and CH_4 on celestial bodies (planets, moons, comets). *Astrobiology*, *15*(7), 587–600. https://doi.org/10.1089/ast.2014.1188

Johnson, J. W., Oelkers, E. H., & Helgeson, H. C. (1992). SUPCRT92: A software package for calculating the standard molal thermodynamic properties of minerals, gases, aqueous species, and reactions from 1 to 5000 bar and 0 to 1000°C. *Computers & Geosciences*, *18*(7), 899–947. https://doi.org/10.1016/0098-3004(92)90029-Q

Kelemen, P., Al Rajhi, A., Godard, M., Ildefonse, B., Köpke, J., MacLeod, C., Manning, C., Michibayashi, K., Nasir, S., Shock, E., Takazawa, E., & Teagle, D. (2013). Scientific drilling and related research in the Samail Ophiolite, Sultanate of Oman. *Scientific Drilling*, *15*, 64–71. https://doi.org/10.5194/sd-15-64-2013

Kelemen, P. B., & Matter, J. (2008). In situ carbonation of peridotite for CO_2 storage.

Proceedings of the National Academy of Sciences, *105*(45), 17295–17300. https://doi.org/10.1073/pnas.0805794105

Kelemen, P. B., Matter, J., Streit, E. E., Rudge, J. F., Curry, W. B., & Blusztajn, J. (2011). Rates and mechanisms of mineral carbonation in peridotite: Natural processes and recipes for enhanced, in situ CO_2 capture and storage. *Annual Review of Earth and Planetary Sciences*, *39*(1), 545–576. https://doi.org/10.1146/annurev-earth-092010-152509

Kelley, D. S., Karson, J. A., Blackman, D. K., Früh-Green, G. L., Butterfield, D. A., Lilley, M. D., Olson, E. J., Schrenk, M. O., Roe, K. K., Lebon, G. T., Rivizzigno, P., & the AT3-60 Shipboard Party. (2001). An off-axis hydrothermal vent field near the Mid-Atlantic Ridge at 30° N. *Nature*, *412*(6843), 145–149. https://doi.org/10.1038/35084000

Khoury, H. N., Salameh, E., Clark, I. D., Fritz, P., Bajjali, W., Milodowski, A. E., Cave, M. R., & Alexander, W. R. (1992). A natural analogue of high pH cement pore waters from the Maqarin area of northern Jordan. I: Introduction to the site. *Journal of Geochemical Exploration*, *46*(1), 117–132. https://doi.org/10.1016/0375-6742(92)90103-F

Khoury, H. N., Salameh, E., & Abdul-Jaber, Q. (1985). Characteristics of an unusual highly alkaline water from the Maqarin area, northern Jordan. *Journal of Hydrology*, *81*(1), 79–91. https://doi.org/10.1016/0022-1694(85)90168-4

Klein, F., Bach, W., & McCollom, T. M. (2013). Compositional controls on hydrogen generation during serpentinization of ultramafic rocks. *Lithos*, *178*, 55–69. https://doi.org/10.1016/j.lithos.2013.03.008

Klein, F., Humphris, S. E., Guo, W., Schubotz, F., Schwarzenbach, E. M., & Orsi, W. D. (2015). Fluid mixing and the deep biosphere of a fossil Lost City-type hydrothermal system at the Iberia Margin. *Proceedings of the National Academy of Sciences*, *112*(39), 12036–12041.

https://doi.org/10.1073/pnas.1504674112

Lang, S. Q., Butterfield, D. A., Schulte, M., Kelley, D. S., & Lilley, M. D. (2010). Elevated concentrations of formate, acetate and dissolved organic carbon found at the Lost City hydrothermal field. *Geochimica et Cosmochimica Acta*, *74*(3), 941–952. https://doi.org/10.1016/j.gca.2009.10.045

Leong, J. A. M., & Shock, E. L. (2020). Thermodynamic constraints on the geochemistry of low-temperature, continental, serpentinization-generated fluids. *American Journal of Science*, *320*(3), 185–235. https://doi.org/10.2475/03.2020.01

Lindsay, M. R., Amenabar, M. J., Fecteau, K. M., Debes, R. V., Martins, M. C. F., Fristad, K. E., Xu, H., Hoehler, T. M., Shock, E. L., & Boyd, E. S. (2018). Subsurface processes influence oxidant availability and chemoautotrophic hydrogen metabolism in Yellowstone hot springs. *Geobiology*, *16*(6), 674–692. https://doi.org/10.1111/gbi.12308

Maher, K. (2010). The dependence of chemical weathering rates on fluid residence time. *Earth and Planetary Science Letters*, *294*(1), 101–110. https://doi.org/10.1016/j.epsl.2010.03.010

Malvoisin, B. (2015). Mass transfer in the oceanic lithosphere: Serpentinization is not isochemical. *Earth and Planetary Science Letters*, *430*, 75–85. https://doi.org/10.1016/j.epsl.2015.07.043

Marques, J. M., Carreira, P. M., Carvalho, M. R., Matias, M. J., Goff, F. E., Basto, M. J., Graça, R. C., Aires-Barros, L., & Rocha, L. (2008). Origins of high pH mineral waters from ultramafic rocks, Central Portugal. *Applied Geochemistry*, *23*(12), 3278–3289. https://doi.org/10.1016/j.apgeochem.2008.06.029

Martin, W., & Russell, M. J. (2007). On the origin of biochemistry at an alkaline hydrothermal

vent. *Philosophical Transactions of the Royal Society B: Biological Sciences*, *362*(1486), 1887–1926. https://doi.org/10.1098/rstb.2006.1881

Martin, W., Baross, J., Kelley, D., & Russell, M. J. (2008). Hydrothermal vents and the origin of life. *Nature Reviews Microbiology*, *6*(11), 805–814. https://doi.org/10.1038/nrmicro1991

Matter, J. M., Waber, H. N., Loew, S., & Matter, A. (2006). Recharge areas and geochemical evolution of groundwater in an alluvial aquifer system in the Sultanate of Oman. *Hydrogeology Journal*, *14*(1), 203–224. https://doi.org/10.1007/s10040-004-0425-2

Matter, J. M., & Kelemen, P. B. (2009). Permanent storage of carbon dioxide in geological reservoirs by mineral carbonation. *Nature Geoscience*, *2*(12), 837–841. https://doi.org/10.1038/ngeo683

Mayhew, L. E., Ellison, E. T., Miller, H. M., Kelemen, P. B., & Templeton, A. S. (2018). Iron transformations during low temperature alteration of variably serpentinized rocks from the Samail ophiolite, Oman. *Geochimica et Cosmochimica Acta*, *222*, 704–728. https://doi.org/10.1016/j.gca.2017.11.023

McCollom, T. M. (2007). Geochemical constraints on sources of metabolic energy for chemolithoautotrophy in ultramafic-hosted deep-sea hydrothermal systems. *Astrobiology*, *7*(6), 933–950. https://doi.org/10.1089/ast.2006.0119

McCollom, T. M. (2016). Abiotic methane formation during experimental serpentinization of olivine. *Proceedings of the National Academy of Sciences*, *113*(49), 13965–13970. https://doi.org/10.1073/pnas.1611843113

McCollom, T. M., & Donaldson, C. (2016). Generation of hydrogen and methane during experimental low-temperature reaction of ultramafic rocks with water. *Astrobiology*, *16*(6), 389–406. https://doi.org/10.1089/ast.2015.1382

McCollom, T. M., & Seewald, J. S. (2007). Abiotic synthesis of organic compounds in deep-sea hydrothermal environments. *Chemical Reviews, 107*(2), 382–401. https://doi.org/10.1021/cr0503660

Mervine, E. M., Humphris, S. E., Sims, K. W. W., Kelemen, P. B., & Jenkins, W. J. (2014). Carbonation rates of peridotite in the Samail Ophiolite, Sultanate of Oman, constrained through 14C dating and stable isotopes. *Geochimica et Cosmochimica Acta, 126*, 371–397. https://doi.org/10.1016/j.gca.2013.11.007

Meyer-Dombard, D. R., Woycheese, K. M., Yargıçoğlu, E. N., Cardace, D., Shock, E. L., Güleçal-Pektas, Y., & Temel, M. (2015). High pH microbial ecosystems in a newly discovered, ephemeral, serpentinizing fluid seep at Yanartaş (Chimera), Turkey. *Frontiers in Microbiology, 5*, no. 723. https://doi.org/10.3389/fmicb.2014.00723

Miller, H. M., Matter, J. M., Kelemen, P., Ellison, E. T., Conrad, M. E., Fierer, N., Ruchala, T., Tominaga, M., & Templeton, A. S. (2016). Modern water/rock reactions in Oman hyperalkaline peridotite aquifers and implications for microbial habitability. *Geochimica et Cosmochimica Acta, 179*, 217–241. https://doi.org/10.1016/j.gca.2016.01.033

Miller, H. M., Chaudhry, N., Conrad, M. E., Bill, M., Kopf, S. H., & Templeton, A. S. (2018). Large carbon isotope variability during methanogenesis under alkaline conditions. *Geochimica et Cosmochimica Acta, 237*, 18–31. https://doi.org/10.1016/j.gca.2018.06.007

Mottl, M. J. (2009). Highest pH. *Geochemical News*.

Mottl, M. J., Komor, S. C., Fryer, P., & Moyer, C. L. (2003). Deep-slab fluids fuel extremophilic Archaea on a Mariana forearc serpentinite mud volcano: Ocean Drilling Program Leg 195. *Geochemistry, Geophysics, Geosystems, 4*(11), no. 9009.

https://doi.org/10.1029/2003GC000588

Mottl, M. J., Wheat, C. G., Fryer, P., Gharib, J., & Martin, J. B. (2004). Chemistry of springs across the Mariana forearc shows progressive devolatilization of the subducting plate. *Geochimica et Cosmochimica Acta*, *68*(23), 4915–4933. https://doi.org/10.1016/j.gca.2004.05.037

National Academies of Sciences, Engineering, and Medicine. (2019). Chapter 6: Carbon Mineralization of CO_2. In *Negative Emissions Technologies and Reliable Sequestration: A Research Agenda* (pp. 247–318). Washington, D.C.: National Academies Press. https://doi.org/10.17226/25259

Neal, C., & Stanger, G. (1983). Hydrogen generation from mantle source rocks in Oman. *Earth and Planetary Science Letters*, *66*, 315–320. https://doi.org/10.1016/0012-821X(83)90144-9

Neal, C., & Stanger, G. (1984). Calcium and magnesium hydroxide precipitation from alkaline groundwaters in Oman, and their significance to the process of serpentinization. *Mineralogical Magazine*, *48*(347), 237–241. https://doi.org/10.1180/minmag.1984.048.347.07

Neal, C., & Stanger, G. (1985). Past and present serpentinisation of ultramafic rocks; an example from the Semail Ophiolite Nappe of Northern Oman. In *The Chemistry of Weathering* (pp. 249–275). Springer.

Nesbitt, H. W., & Bricker, O. P. (1978). Low temperature alteration processes affecting ultramafic bodies. *Geochimica et Cosmochimica Acta*, *42*(4), 403–409. https://doi.org/10.1016/0016-7037(78)90271-5

Nicolas, A., Boudier, F., Ildefonse, B., & Ball, E. (2000). Accretion of Oman and United Arab

1344 Emirates ophiolite – Discussion of a new structural map. *Marine Geophysical*
1345 *Researches*, *21*(3), 147–180. https://doi.org/10.1023/A:1026769727917
1346 Nordstrom, K. D., McCleskey, B. R., & Ball, J. W. (2009). Sulfur geochemistry of hydrothermal
1347 waters in Yellowstone National Park: IV Acid–sulfate waters. *Applied Geochemistry*,
1348 *24*(2), 191–207. https://doi.org/10.1016/j.apgeochem.2008.11.019
1349 de Obeso, J. C., & Kelemen, P. B. (2018). Fluid rock interactions on residual mantle peridotites
1350 overlain by shallow oceanic limestones: Insights from Wadi Fins, Sultanate of Oman.
1351 *Chemical Geology*, *498*, 139–149. https://doi.org/10.1016/j.chemgeo.2018.09.022
1352 de Obeso, J. C., & Kelemen, P. B. (2020). Major element mobility during serpentinization,
1353 oxidation and weathering of mantle peridotite at low temperatures. *Philosophical*
1354 *Transactions of the Royal Society A: Mathematical, Physical and Engineering Sciences*,
1355 *378*(2165), 20180433. https://doi.org/10.1098/rsta.2018.0433
1356 Oelkers, E. H., & Schott, J. (2001). An experimental study of enstatite dissolution rates as a
1357 function of pH, temperature, and aqueous Mg and Si concentration, and the mechanism
1358 of pyroxene/pyroxenoid dissolution. *Geochimica et Cosmochimica Acta*, *65*(8), 1219–
1359 1231. https://doi.org/10.1016/S0016-7037(00)00564-0
1360 Ohlsson, J. I., Osvatic, J. T., Becraft, E. D., & Swingley, W. D. (2019). Microbial community in
1361 hyperalkaline steel slag-fill emulates serpentinizing springs. *Diversity*, *11*(7), 103.
1362 https://doi.org/10.3390/d11070103
1363 Okland, I., Huang, S., Dahle, H., Thorseth, I. H., & Pedersen, R. B. (2012). Low temperature
1364 alteration of serpentinized ultramafic rock and implications for microbial life. *Chemical*
1365 *Geology*, *318–319*, 75–87. https://doi.org/10.1016/j.chemgeo.2012.05.015
1366 Olsson, J., Stipp, S. L. S., & Gislason, S. R. (2015). Element scavenging by recently formed

travertine deposits in the alkaline springs from the Oman Semail Ophiolite. *Mineralogical Magazine*, *78*(6), 1479–1490. https://doi.org/10.1180/minmag.2014.078.6.15

Palandri, J. L., & Reed, M. H. (2004). Geochemical models of metasomatism in ultramafic systems: serpentinization, rodingitization, and sea floor carbonate chimney precipitation. *Geochimica et Cosmochimica Acta*, *68*(5), 1115–1133. https://doi.org/10.1016/j.gca.2003.08.006

Paukert, A. N., Matter, J. M., Kelemen, P. B., Shock, E. L., & Havig, J. R. (2012). Reaction path modeling of enhanced in situ CO_2 mineralization for carbon sequestration in the peridotite of the Samail Ophiolite, Sultanate of Oman. *Chemical Geology*, *330–331*, 86–100. https://doi.org/10.1016/j.chemgeo.2012.08.013

Paukert Vankeuren, A. N., Matter, J. M., Stute, M., & Kelemen, P. B. (2019). Multitracer determination of apparent groundwater ages in peridotite aquifers within the Samail ophiolite, Sultanate of Oman. *Earth and Planetary Science Letters*, *516*, 37–48. https://doi.org/10.1016/j.epsl.2019.03.007

Pedersen, K., Nilsson, E., Arlinger, J., Hallbeck, L., & O'Neill, A. (2004). Distribution, diversity and activity of microorganisms in the hyper-alkaline spring waters of Maqarin in Jordan. *Extremophiles*, *8*(2), 151–164. https://doi.org/10.1007/s00792-004-0374-7

Pfeifer, H. R. (1977). A model for fluids in metamorphosed ultramafic rocks : observations at surface and subsurface conditions (high pH spring waters). *Schweizerische Mineralogische Und Petrographische Mitteilungen*, *57*(3), 361–396. https://doi.org/10.5169/seals-44441

Pokrovsky, O. S., & Schott, J. (1999). Processes at the magnesium-bearing carbonates/solution

1390 interface. II. Kinetics and mechanism of magnesite dissolution. *Geochimica et*
1391 *Cosmochimica Acta*, *63*(6), 881–897. https://doi.org/10.1016/S0016-7037(99)00013-7
1392 Pokrovsky, O. S., & Schott, J. (2000). Kinetics and mechanism of forsterite dissolution at 25°C
1393 and pH from 1 to 12. *Geochimica et Cosmochimica Acta*, *64*(19), 3313–3325.
1394 https://doi.org/10.1016/S0016-7037(00)00434-8
1395 Pokrovsky, O. S., & Schott, J. (2004). Experimental study of brucite dissolution and precipitation
1396 in aqueous solutions: surface speciation and chemical affinity control. *Geochimica et*
1397 *Cosmochimica Acta*, *68*(1), 31–45. https://doi.org/10.1016/S0016-7037(03)00238-2
1398 Rempfert, K. R., Miller, H. M., Bompard, N., Nothaft, D., Matter, J. M., Kelemen, P., Fierer, N.,
1399 & Templeton, A. S. (2017). Geological and geochemical controls on subsurface
1400 microbial life in the Samail Ophiolite, Oman. *Frontiers in Microbiology*, *8*, no. 56.
1401 https://doi.org/10.3389/fmicb.2017.00056
1402 Roadcap, G. S., Kelly, W. R., & Bethke, C. M. (2005). Geochemistry of extremely alkaline (pH
1403 >12) ground water in slag-fill aquifers. *Groundwater*, *43*(6), 806–816.
1404 https://doi.org/10.1111/j.1745-6584.2005.00060.x
1405 Robinson, K. J. (2017). *Modeling Aqueous Organic Chemistry in Experimental and Natural*
1406 *Systems*. Arizona State University, Tempe, AZ.
1407 Russell, M. J., Daniel, R. M., Hall, A. J., & Sherringham, J. A. (1994). A hydrothermally
1408 precipitated catalytic iron sulphide membrane as a first step toward life. *Journal of*
1409 *Molecular Evolution*, *39*(3), 231–243. https://doi.org/10.1007/BF00160147
1410 Russell, M. J., Hall, A. J., & Martin, W. (2010). Serpentinization as a source of energy at the
1411 origin of life. *Geobiology*, *8*(5), 355–371. https://doi.org/10.1111/j.1472-
1412 4669.2010.00249.x

1413 Russell, M. J. (2018). Green Rust: The simple organizing 'seed' of all life? *Life*, *8*(3), no. 35.
1414 https://doi.org/10.3390/life8030035
1415 Sader, J. A., Leybourne, M. I., McClenaghan, M. B., & Hamilton, S. M. (2007). Low-
1416 temperature serpentinization processes and kimberlite groundwater signatures in the
1417 Kirkland Lake and Lake Timiskiming kimberlite fields, Ontario, Canada: implications for
1418 diamond exploration. *Geochemistry: Exploration, Environment, Analysis*, *7*(1), 3–21.
1419 https://doi.org/10.1144/1467-7873/06-900
1420 Sano, Y., Urabe, A., Wakita, H., & Wushiki, H. (1993). Origin of hydrogen-nitrogen gas seeps,
1421 Oman. *Applied Geochemistry*, *8*(1), 1–8. https://doi.org/10.1016/0883-2927(93)90053-J
1422 Schrenk, M. O., Brazelton, W. J., & Lang, S. Q. (2013). Serpentinization, carbon, and deep life.
1423 *Reviews in Mineralogy and Geochemistry*, *75*(1), 575–606.
1424 https://doi.org/10.2138/rmg.2013.75.18
1425 Schulte, M., Blake, D., Hoehler, T., & McCollom, T. (2006). Serpentinization and its
1426 Implications for life on the Early Earth and Mars. *Astrobiology*, *6*(2), 364–376.
1427 https://doi.org/10.1089/ast.2006.6.364
1428 Schwarzenbach, E. M., Lang, S. Q., Früh-Green, G. L., Lilley, M. D., Bernasconi, S. M., &
1429 Méhay, S. (2013). Sources and cycling of carbon in continental, serpentinite-hosted
1430 alkaline springs in the Voltri Massif, Italy. *Lithos*, *177*, 226–244.
1431 https://doi.org/10.1016/j.lithos.2013.07.009
1432 Shock, E., & Canovas, P. (2010). The potential for abiotic organic synthesis and biosynthesis at
1433 seafloor hydrothermal systems. *Geofluids*, *10*(1–2), 161–192.
1434 https://doi.org/10.1111/j.1468-8123.2010.00277.x
1435 Shock, E. L. (1992). Chemical environments of submarine hydrothermal systems. In N. G. Holm

(Ed.), *Marine Hydrothermal Systems and the Origin of Life: Report of SCOR Working Group 91* (pp. 67–107). Dordrecht: Springer Netherlands. https://doi.org/10.1007/978-94-011-2741-7_5

Shock, E. L., & Helgeson, H. C. (1988). Calculation of the thermodynamic and transport properties of aqueous species at high pressures and temperatures: Correlation algorithms for ionic species and equation of state predictions to 5 kb and 1000°C. *Geochimica et Cosmochimica Acta*, *52*(8), 2009–2036. https://doi.org/10.1016/0016-7037(88)90181-0

Shock, E. L., Helgeson, H. C., & Sverjensky, D. A. (1989). Calculation of the thermodynamic and transport properties of aqueous species at high pressures and temperatures: Standard partial molal properties of inorganic neutral species. *Geochimica et Cosmochimica Acta*, *53*(9), 2157–2183. https://doi.org/10.1016/0016-7037(89)90341-4

Shock, E. L., Oelkers, E. H., Johnson, J. W., Sverjensky, D. A., & Helgeson, H. C. (1992). Calculation of the thermodynamic properties of aqueous species at high pressures and temperatures. Effective electrostatic radii, dissociation constants and standard partial molal properties to 1000 C and 5 kbar. *Journal of the Chemical Society, Faraday Transactions*, *88*(6), 803–826. https://doi.org/10.1039/FT9928800803

Shock, E. L., Sassani, D. C., Willis, M., & Sverjensky, D. A. (1997). Inorganic species in geologic fluids: Correlations among standard molal thermodynamic properties of aqueous ions and hydroxide complexes. *Geochimica et Cosmochimica Acta*, *61*(5), 907–950. https://doi.org/10.1016/S0016-7037(96)00339-0

Sleep, N. H., Meibom, A., Fridriksson, T., Coleman, R. G., & Bird, D. K. (2004). H_2-rich fluids from serpentinization: Geochemical and biotic implications. *Proceedings of the National Academy of Sciences*, *101*(35), 12818–12823. https://doi.org/10.1073/pnas.0405289101

1459 Stanger, G. (1986). *The hydrogeology of the Oman Mountains*. The Open University, UK.
1460 St-Jean, G. (2003). Automated quantitative and isotopic (^{13}C) analysis of dissolved inorganic
1461 carbon and dissolved organic carbon in continuous-flow using a total organic carbon
1462 analyser. *Rapid Communications in Mass Spectrometry*, *17*(5), 419–428.
1463 https://doi.org/10.1002/rcm.926
1464 Suda, K., Ueno, Y., Yoshizaki, M., Nakamura, H., Kurokawa, K., Nishiyama, E., Yoshino, K.,
1465 Hongoh, Y., Kawachi, K., Omori, S., Yamada, K., Yoshida, N., & Maruyama, S. (2014).
1466 Origin of methane in serpentinite-hosted hydrothermal systems: The CH_4–H_2–H_2O
1467 hydrogen isotope systematics of the Hakuba Happo hot spring. *Earth and Planetary*
1468 *Science Letters*, *386*, 112–125. https://doi.org/10.1016/j.epsl.2013.11.001
1469 Sverjensky, D. A., Shock, E. L., & Helgeson, H. C. (1997). Prediction of the thermodynamic
1470 properties of aqueous metal complexes to 1000°C and 5 kb. *Geochimica et*
1471 *Cosmochimica Acta*, *61*(7), 1359–1412. https://doi.org/10.1016/S0016-7037(97)00009-4
1472 Szponar, N., Brazelton, W. J., Schrenk, M. O., Bower, D. M., Steele, A., & Morrill, P. L. (2013).
1473 Geochemistry of a continental site of serpentinization, the Tablelands Ophiolite, Gros
1474 Morne National Park: A Mars analogue. *Icarus*, *224*(2), 286–296.
1475 https://doi.org/10.1016/j.icarus.2012.07.004
1476 Taylor, H. P. (1974). The application of oxygen and hydrogen isotope studies to problems of
1477 hydrothermal alteration and ore deposition. *Economic Geology*, *69*(6), 843–883.
1478 https://doi.org/10.2113/gsecongeo.69.6.843
1479 Taylor, R. M., Hansen, H. C. B., Stanger, G., & Koch, C. B. (1991). On the genesis and
1480 composition of natural pyroaurite. *Clay Minerals*, *26*(3), 297–309.
1481 https://doi.org/10.1180/claymin.1991.026.3.01

1482 Templeton, A. S., & Ellison, E. T. (2020). Formation and loss of metastable brucite: does Fe(II)-
1483 bearing brucite support microbial activity in serpentinizing ecosystems? *Philosophical*
1484 *Transactions of the Royal Society A: Mathematical, Physical and Engineering Sciences*,
1485 *378*(2165), 20180423. https://doi.org/10.1098/rsta.2018.0423
1486 Thom, J. G. M., Dipple, G. M., Power, I. M., & Harrison, A. L. (2013). Chrysotile dissolution
1487 rates: Implications for carbon sequestration. *Applied Geochemistry*, *35*, 244–254.
1488 https://doi.org/10.1016/j.apgeochem.2013.04.016
1489 Tutolo, B. M., Luhmann, A. J., Tosca, N. J., & Seyfried, W. E. (2018). Serpentinization as a
1490 reactive transport process: The brucite silicification reaction. *Earth and Planetary*
1491 *Science Letters*, *484*, 385–395. https://doi.org/10.1016/j.epsl.2017.12.029
1492 Vacquand, C., Deville, E., Beaumont, V., Guyot, F., Sissmann, O., Pillot, D., Arcilla, C., &
1493 Prinzhofer, A. (2018). Reduced gas seepages in ophiolitic complexes: Evidences for
1494 multiple origins of the H_2-CH_4-N_2 gas mixtures. *Geochimica et Cosmochimica Acta*, *223*,
1495 437–461. https://doi.org/10.1016/j.gca.2017.12.018
1496 Vance, S., Harnmeijer, J., Kimura, J., Hussmann, H., de Martin, B., & Brown, J. M. (2007).
1497 Hydrothermal systems in small ocean planets. *Astrobiology*, *7*(6), 987–1005.
1498 https://doi.org/10.1089/ast.2007.0075
1499 Velbel, M. A. (1993). Constancy of silicate-mineral weathering-rate ratios between natural and
1500 experimental weathering: implications for hydrologic control of differences in absolute
1501 rates. *Chemical Geology*, *105*(1), 89–99. https://doi.org/10.1016/0009-2541(93)90120-8
1502 Waite, J. H., Glein, C. R., Perryman, R. S., Teolis, B. D., Magee, B. A., Miller, G., Grimes, J.,
1503 Perry, M. E., Miller, K. E., Bouquet, A., Lunine, J. I., Brockwell, T., & Bolton, S. J.
1504 (2017). Cassini finds molecular hydrogen in the Enceladus plume: Evidence for

hydrothermal processes. *Science*, *356*(6334), 155–159. https://doi.org/10.1126/science.aai8703

Wang, D. T., Reeves, E. P., McDermott, J. M., Seewald, J. S., & Ono, S. (2018). Clumped isotopologue constraints on the origin of methane at seafloor hot springs. *Geochimica et Cosmochimica Acta*, *223*, 141–158. https://doi.org/10.1016/j.gca.2017.11.030

Weyhenmeyer, C. E., Burns, S. J., Waber, H. N., Macumber, P. G., & Matter, A. (2002). Isotope study of moisture sources, recharge areas, and groundwater flow paths within the eastern Batinah coastal plain, Sultanate of Oman. *Water Resources Research*, *38*(10), no. 1184. https://doi.org/10.1029/2000WR000149

Wheat, C. G., Fryer, P., Fisher, A. T., Hulme, S., Jannasch, H., Mottl, M. J., & Becker, K. (2008). Borehole observations of fluid flow from South Chamorro Seamount, an active serpentinite mud volcano in the Mariana forearc. *Earth and Planetary Science Letters*, *267*(3), 401–409. https://doi.org/10.1016/j.epsl.2007.11.057

Wheat, C. G., Seewald, J. S., & Takai, K. (2020). Fluid transport and reaction processes within a serpentinite mud volcano: South Chamorro Seamount. *Geochimica et Cosmochimica Acta*, *269*, 413–428. https://doi.org/10.1016/j.gca.2019.10.037

White, A. F., & Brantley, S. L. (2003). The effect of time on the weathering of silicate minerals: why do weathering rates differ in the laboratory and field? *Chemical Geology*, *202*(3), 479–506. https://doi.org/10.1016/j.chemgeo.2003.03.001

Wolery, T., & Jarek, R. (2003). *EQ3/6, Version 8.0, Software User's Manual* (No. 10813- UM-8.0– 00) (p. 376). Las Vegas, Nevada: US Department of Energy, Office of Civilian Radioactive Waste Management, Office of Repository Development.

Wolery, T. J., & Jove-Colon, C. F. (2004). *Qualification of thermodynamic data for geochemical*

modeling of mineral-water interactions in dilute systems (No. ANL-WIS-GS-000003) (p. 212). Las Vegas, Nevada: US Department of Energy, Office of Civilian Radioactive Waste Management, Office of Repository Development.

Yuce, G., Italiano, F., D'Alessandro, W., Yalcin, T. H., Yasin, D. U., Gulbay, A. H., Ozyurt, N. N., Rojay, B., Karabacak, V., Bellomo, S., Brusca, L., Yang, T., Fu, C. C., Lai, C. W., Ozacar, A., & Walia, V. (2014). Origin and interactions of fluids circulating over the Amik Basin (Hatay, Turkey) and relationships with the hydrologic, geologic and tectonic settings. *Chemical Geology*, *388*, 23–39. https://doi.org/10.1016/j.chemgeo.2014.09.006

Zgonnik, V., Beaumont, V., Larin, N., Pillot, D., & Deville, E. (2019). Diffused flow of molecular hydrogen through the Western Hajar mountains, Northern Oman. *Arabian Journal of Geosciences*, *12*(3), no. 71. https://doi.org/10.1007/s12517-019-4242-2